# aDISCO: A Broadly Applicable Method for 3D Microscopy of Archival Paraffin-Embedded Human Tissues

Anna Maria Reuss[1,4*], Peter Rupprecht[2,4], Dominik Groos[2], Martina Cerisoli[1], Lena Nordberg[1], Lukas Frick[1], Fabian F. Voigt[2,3], Nikita Vladimirov[2,5], Philipp Bethge[2], Regina Reimann[1], Fritjof Helmchen[2,4,5], Adriano Aguzzi[1,4*]

[1]Institute of Neuropathology, University of Zurich, Schmelzbergstrasse 12, 8091 Zurich, Switzerland

[2] Brain Research Institute, University of Zurich, Winterthurerstrasse 190, 8057 Zurich, Switzerland

[3] Current address: Department of Molecular and Cellular Biology, Harvard University, Cambridge, MA, USA

[4]Neuroscience Center Zurich, University of Zurich, Winterthurerstrasse 190, 8057 Zurich, Switzerland

[5]University Research Priority Program (URPP), Adaptive Brain Circuits in Development and Learning, University of Zurich, Zurich, Switzerland

*Correspondence: annamaria.reuss@uzh.ch; adriano.aguzzi@uzh.ch

## Abstract

During human surgeries and autopsies, specimens are regularly sampled and stored as formalin-fixed paraffin-embedded (FFPE) tissue blocks. Diagnoses are rendered by microscopical examination of two-dimensional sections. Good clinical practice requires that samples be retained for decades, thus giving rise to enormous archives of healthy and diseased human tissues. Tissue-clearing technologies and whole-mount microscopy would enable 3D analyses, but whole FFPE tissue blocks are often unsuitable for clearing due to their size, their extensive covalent cross-linking, and their embedding in solid wax. Here, we present ‘archival DISCO’ (aDISCO), a versatile and robust clearing method for whole-mount archival FFPE human tissue blocks. aDISCO enabled complete clearing and consistent antibody staining of samples stored for at least 15 years. We show that aDISCO can be applied to human brain, spinal cord, peripheral nerve, skin, muscle, heart, kidney, liver, spleen, colon, and lung, and is compatible with a wide range of commonly used antibodies. We applied aDISCO to the 3D study of focal cortical dysplasia (FCD), a neurodevelopmental disease associated with epilepsy. We performed deep-learning-based segmentation and object detection to identify both focal and global neuronal density variations in FCD and to precisely quantify the disruption of cortical layering, features that are likely to be overlooked by conventional histology. When combined with selective-plane illumination microscopy, aDISCO delivers natively digital data suitable for deep-learning-based processing, thus enabling the detection of subtle and sparse pathologies in large archival human tissue specimens.

## Introduction

Histology is an important tool for the diagnosis of diseases and for biological research[1, 2]. Formalin-fixed, paraffin-embedded (FFPE) tissue preservation was pioneered by Ferdinand Blum in 1893[3] and became widely adopted in the early 20th century. FFPE tissue blocks are usually sliced into thin sections measuring about 5 µm (ref. [4]). FFPE histology produces optically clear sections accessible to transmission light microscopy. However, such analyses are intrinsically two-dimensional and enable examination of only a small fraction of the tissue sample. This, in turn, may prevent the detection of important pathologies and can only partially be obviated by the laborious scrutiny of numerous layered sections. These limitations impair the evaluation of spatially complex, convoluted structures such as blood vessels and nerve fibers.

3D histology has the potential to transcend the limitations described above. However, it requires transparency of thick tissue blocks, since the opacity inherent to most biological tissues (resulting from light scattering, pigmentation, and opalescence of tissue) impedes microscopic examination[5]. To overcome these physical limitations, lipids (a major source of refraction inhomogeneity and light scattering) are removed, and refractive indices (RIs) are matched to the immersion medium. While various tissue clearing methods were invented and have evolved in recent years, human tissue clearing presents unique challenges[6].

Since the dimensions of human organs exceed those of common model organisms, human tissue samples can be large. For example, conventional FFPE human tissue blocks with dimensions of up to 20 x 15 x 7 $mm^3$ exceed the size of an entire mouse brain. In particular, tissues rich in lipids and collagen such as brain white matter and liver are difficult to clear and stain effectively[7-9]. Also, tissue fibrosis, which increases physiologically with age, makes sample preparation from aged adult patients particularly challenging[10, 11]. Thus, processing human samples for 3D histology must achieve effective clearing without compromising tissue integrity and must enable complete antibody diffusion without staining gradients towards the center of the tissue specimen. Both issues are particularly challenging in archival FFPE tissue due to aldehyde cross-linking and epitope masking through formalin fixation, dehydration, and paraffin substitution[12]. Moreover, immunofluorescent staining of human samples entails additional issues such as autofluorescence from pigments like lipofuscin, melanin, or coagulated blood, which can disturb the desired signals[6]. For these reasons, current human tissue clearing methods with successful immunolabeling are limited to either small (< 2 mm) FFPE samples or freshly processed samples from few organs, primarily from the brain[13-28] (Extended Data Table 1). A robust 3D histology pipeline for effective clearing and immunolabeling of large, long-term-stored FFPE human tissue specimens that is applicable across various organs and coupled with a validated set of antibodies has not been developed yet.

Here, we introduce 'archival DISCO' (aDISCO), a versatile and robust clearing method designed to achieve effective clearing and antibody staining in whole-mount FFPE human tissue blocks from diagnostic archives, thereby making vast collections of human tissue samples available for deeper investigation. We demonstrate the suitability of aDISCO across different human organs and its compatibility with a large set of antibodies, obtaining 3D whole-mount images at various magnification using light-sheet fluorescence microscopy (mesoSPIM version (V)5 and V6)[29, 30]. In a use-case study based on a relatively rare pathological condition (focal cortical dysplasia, FCD), we demonstrate that 3D histology with aDISCO produces high-quality data that can be processed with automated segmentation and object detection methods based on deep-learning. These results showcase the potential of 3D histology with aDISCO to detect subtle and focal pathologies in large archival human tissue specimens.

## Results

### *Development of aDISCO*

We developed a clearing protocol that enables the processing of long-term-stored (samples used in this study stored for 11-15 years) standard FFPE tissue blocks from various human organs, which are customarily stored in diagnostic archives for surgical pathology, autoptic pathology, and at institutes of human anatomy (Fig. 1a). The method presented here is based on three main innovations: (1) harsh clearing with a combination of tetrahydrofuran (THF) and dichloromethane (DCM), (2) strong autofluorescence suppression using acidic cupric sulfate in ammonium acetate, and (3) gradual antibody staining with increasing antibody concentrations.

Standard FFPE human tissue blocks are relatively large (up to 20 x 15 x 7 $mm^3$, depending on sampling and prior cutting) and various tissues including skin, liver, and white matter-rich regions of the brain are additionally very dense[8, 9, 31]. To strike a balance between effective clearing and preservation of tissue integrity, we applied a novel combination of the polar and organic solvents THF and DCM. These chemicals are used repeatedly (Fig. 1a, steps 3, 4, 8) to achieve stepwise delipidation. In addition, pre-clearing loosens the dense tissue, which facilitates antibody penetration for immunolabeling.

Bleaching with hydrogen peroxide, used in previous clearing protocols[10, 15], is often insufficient to suppress autofluorescence from coagulated blood, lipofuscin, melanin, and other pigments[6], even when applied at high concentrations (Extended Data Fig. 1a). This is problematic for automated segmentation during 3D data analysis, because brightly autofluorescent artifacts may be falsely interpreted as positive signals. In aDISCO, we achieved removal of autofluorescent artifacts by additional treatment with acidic cupric sulfate in ammonium acetate, whose effectiveness had been demonstrated on 2D sections

already in the 1990s[32]. However, we found that its application after immunolabeling suppressed the desired staining signal (Extended Data Fig. 1b). Therefore, we applied it before initiating the staining procedure (Fig. 1a, step 5), thus preserving the specific staining signal while removing autofluorescence background (Extended Data Fig. 1b).

Antibody staining in dense, 2-5 mm thick samples, particularly in archival human tissues, has been a major issue in the human tissue clearing field. Therefore, immunolabeling has only been achieved in small FFPE human tissue specimens with limited imaging depth[14, 19, 28] (Extended Data Table 1). Epitopes are often masked in FFPE tissue by overfixation and paraffin embedding, preventing the antibodies from binding to their respective antigens[12]. The aDISCO protocol achieves epitope demasking of antibodies through its combination of deparaffination, pre-clearing, and permeabilization (Fig. 1a). For antibodies yielding weak staining signals, we additionally performed antigen retrieval with formic acid (Fig. 1a, step 5).

To enhance antibody diffusion, we introduced a series of consecutive permeabilization steps before and during the staining procedure by combining various reagents which have been previously shown to facilitate permeabilization[10, 33-35] (Fig. 1a). Each step makes the dense human tissue less compact, thereby preparing it for antibody diffusion.

Most importantly, we noticed that previous clearing protocols used a single antibody concentration, which was often applied at high concentration to reach bright staining signal[13, 14, 17]. However, we observed that in large samples this procedure typically results in a bright rim of stained tissue and insufficient staining inside the tissue, with a visible signal gradient or even a dark center. To prevent accumulation of antibodies at the tissue rim, we employed an approach starting with low antibody concentration, which we gradually increased by adding more and more antibodies to the staining solution (Fig. 1a, step 7). The combination of these innovations enabled reliable clearing and homogeneous immunolabeling, i.e., without obvious staining gradients, of entire FFPE tissue blocks from various human organs and was compatible with a substantial set of commonly used antibodies to characterize these organs.

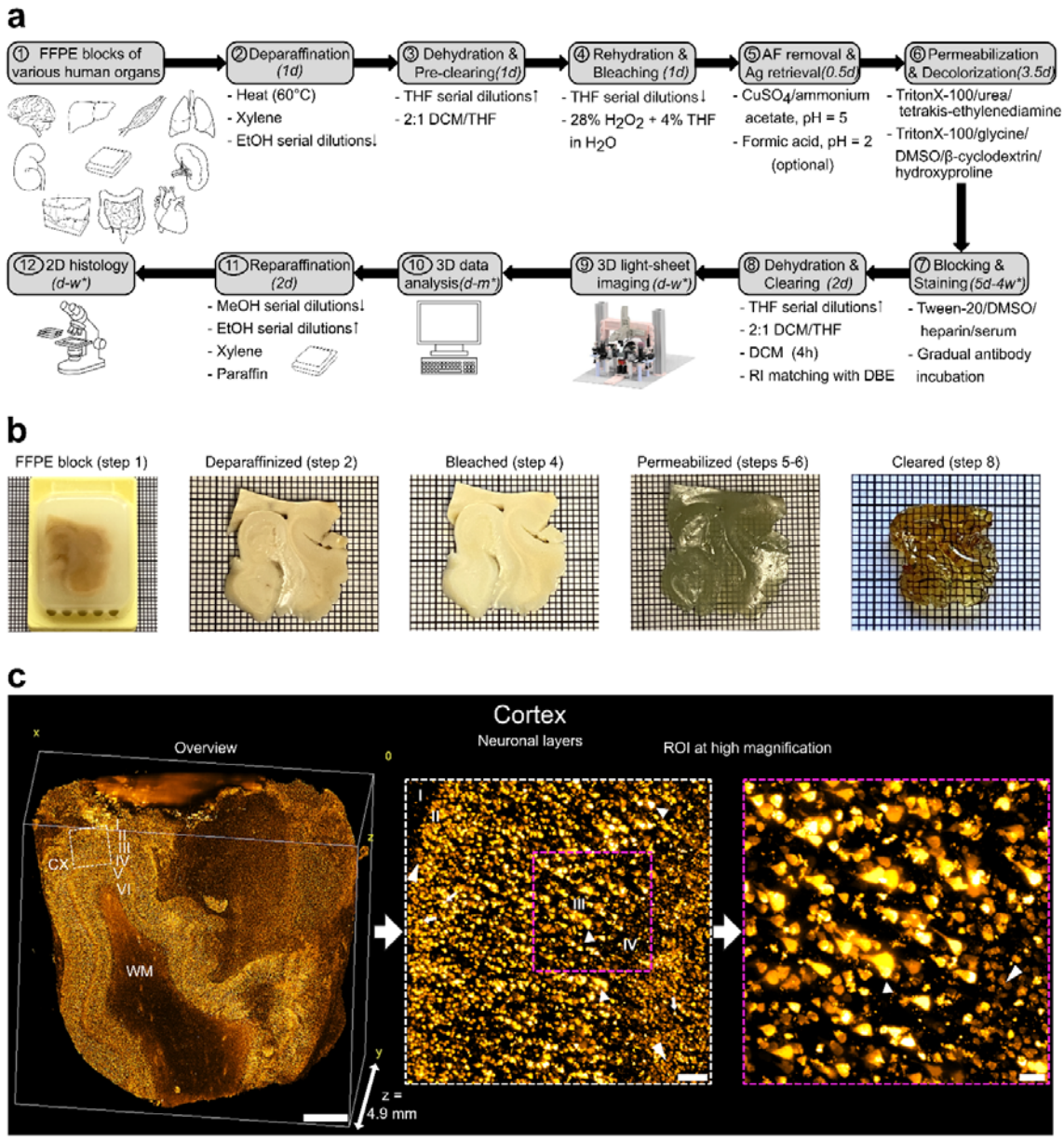


**Figure 1. Overview of the aDISCO protocol for clearing and immunolabeling of archival human tissue blocks.** **a**, The aDISCO pipeline. FFPE human tissue blocks are processed (steps 1-8), imaged using light-sheet microscopy (step 9; mesoSPIM V5 and V6), and analyzed in 3D (step 10). Cleared samples can be reparaffinized (step 11) and reused for conventional 2D histology (step 12). d: days, w: weeks, m: months, FFPE: formalin-fixed paraffin-embedded, EtOH: ethanol, THF: tetrahydrofuran, DCM: dichloromethane, $H_2O_2$: hydrogen peroxide, $H_2O$: water, AF: autofluorescence, Ag: antigen, $CuSO_4$: cupric sulfate, DMSO: dimethylsulfoxide, RI: refractive index, DBE: dibenzylether. **b**, Archival human brain sample after serial procedures as described. Small squares: 1 mm. **c**, Left: 3D rendering of whole-mount archival human brain cortex (CX) sample, stained for neurons (anti-NeuN antibody), and imaged at moderate optical magnification (1.25x) using mesoSPIM V5. Cortical layers I-VI and white matter (WM) are discernable. Scale bar: 2 mm. Middle: High-magnification imaging (12.6x; mesoSPIM V5) of a smaller region-of-interest (ROI) reveals neuronal cytoarchitecture of granular cells (large arrowheads) and small pyramidal cells (arrows) in layers II and IV as well as large pyramidal cells (small arrowheads) in layer III. Scale bar: 100 µm. Right: Further digital zoom into the ROI. Scale bar: 50 µm.

### *Validation of 3D histology with aDISCO-processed whole-mount archival human tissue blocks*

Two-dimensional histology is regarded as a ground-truth provider for human surgical pathology. Validation of 3D findings by 2D histology requires clearing of archival tissue to be compatible with subsequent re-embedding in paraffin, conventional histological processing, and staining (Fig. 1a, steps 11-12). We developed a reparaffination protocol which gently restores the original FFPE tissue block integrity and results in 2D sections with similar staining quality as the original non-cleared FFPE tissue sections (Extended Data Fig. 1c). This will allow for validation of aDISCO against the current standard-of-care, which is a crucial requirement for the licensure and clinical use of novel diagnostic procedures as a complementary method to conventional 2D histology.

Tissue clearing procedures are laborious and can take several weeks depending on sample size. It is therefore helpful to assess their performance at intermediate stages. We performed such quality testing on archival human brain samples during aDISCO processing. After deparaffination (Fig. 1b, steps 1-2), archival human tissue is usually of brownish color, which becomes whitish after successful bleaching (Fig. 1b, step 4) and greenish after cupric-sulfate treatment (Fig. 1b, step 5). After strong permeabilization and decolorization, less compact tissues such as the cortical gray matter of the brain already start becoming transparent, whereas the white matter remains opaque (Fig. 1b, step 6). Final clearing and refractive index (RI) matching render the entire sample fully transparent (Fig. 1b, step 8).

Next, to illustrate and assess the results of the aDISCO protocol, we processed an archival human brain cortex sample which had been stored as FFPE for 15 years. We stained the sample with anti-NeuN antibody which identifies neurons (Fig. 1c, Suppl. Video 1). We chose this sample, since brain cortex is the most frequently cleared human tissue in the literature[13, 15, 17, 19, 20, 22-27]. In a 3D rendering of the whole-mount imaged sample using light-sheet microscopy, the architecture of the human cortex with its six distinct layers was identified and distinguished from the adjacent white matter (Fig.1c, left). Light-sheet imaging of a region-of-interest (ROI) from the same sample with higher magnification (Fig.1c, middle and right) displayed the characteristic cytoarchitecture of pyramidal and granular neurons in distinct layers.

Next, to assess staining and clearing quality across the entire tissue block, we calculated the mean fluorescence intensity (MFI) projection along the z-direction. In the two horizontal directions (x and y), MFI was similar between superficial and deep areas of similar composition (e.g., cortex), with inhomogeneities reflecting region-specific cellular distributions rather than staining gradients (Extended Data Fig. 2a). In addition, we computed the z-profile of mean fluorescence intensity averaged across x and y. The z-profile remained stable throughout the entire range in the vertical (z) direction, even in the center of the sample (Extended Data Fig. 2b). Moreover, slices of the sample center in all three image

projections demonstrated homogeneous staining independent of the acquired imaging plane (Extended Data Fig. 2c).

These results demonstrate that aDISCO achieves effective clearing and immunolabeling of long-term-stored, whole-mount FFPE human tissue blocks, thereby complementing routine 2D diagnostics with 3D histology capabilities. Since the staining quality did not degrade after at least 15 years of storage, aDISCO seems suitable for the investigation of historical samples.

### *3D histology of different human central nervous system (CNS) regions*

Next, we tested the applicability of aDISCO across a broad spectrum of human archival CNS samples (Fig. 2, Suppl. Videos 2, 3). We used various antibody stains and light-sheet microscopy to visualize parvalbumin-positive interneurons in the cortex, IBA1-positive microglia and podocalyxin-positive blood vessels in the hippocampus, tyrosine hydroxylase (TH)-positive dopaminergic neurons in the midbrain, tryptophane hydroxylase (TPH)2-positive serotonergic neurons in the hindbrain, GFAP-positive astrocytes and SMA-positive arterial vessels in the spinal cord, and neurofilament-positive neurons, including Purkinje cells, and nerve fibers in the cerebellum.

Despite the variability of cellular composition across CNS samples and the diversity of antibodies used in this study, stained signal intensities were homogeneous throughout the entire tissue blocks (Fig. 2), which was confirmed by MFI projections (Extended Data Fig. 3). This finding also held true for subcortical brain regions and the spinal cord, containing high amounts of white matter (Fig. 2c-e). In general, imaging depth was not limited by antibody penetration or the quality of clearing but by the size of the respective tissue blocks, which was 8.7 ± 2.8 mm (mean ± s.d. across n = 7 CNS samples) x 7.5 ± 1.9 mm, and 3.7 ± 1.0 mm thick after tissue shrinkage following organic solvent-based tissue clearing[5]. The maximal sample thickness was 4.9 mm (cortex, Fig. 1c).

To further test the clearing quality and the high optical resolution enabled by aDISCO, we imaged smaller ROIs across all processed samples using high-magnification objectives (up to 20x; insets in Figs. 1-3) with a nominal resolution of down to 1.5 µm laterally[30]. In all CNS samples cleared with aDISCO (Figs. 1 and 2), we achieved high resolution throughout the sample, which allowed us to identify individual somata and branched processes of several neuronal cell types (Fig. 2a, c, d, f), the interactions of microglia feet with finely branched blood vessels (Fig. 2b), and the processes of stellate astrocytes in the spinal cord (Fig. 2e). In summary, our results demonstrate effective clearing and staining across large CNS samples, while enabling subcellular resolution of fine structures even deep within each tissue block. Hence, aDISCO yields high-quality 3D data of large archival human samples across the entire CNS spectrum, including cortex, brain stem, cerebellum, and spinal cord.

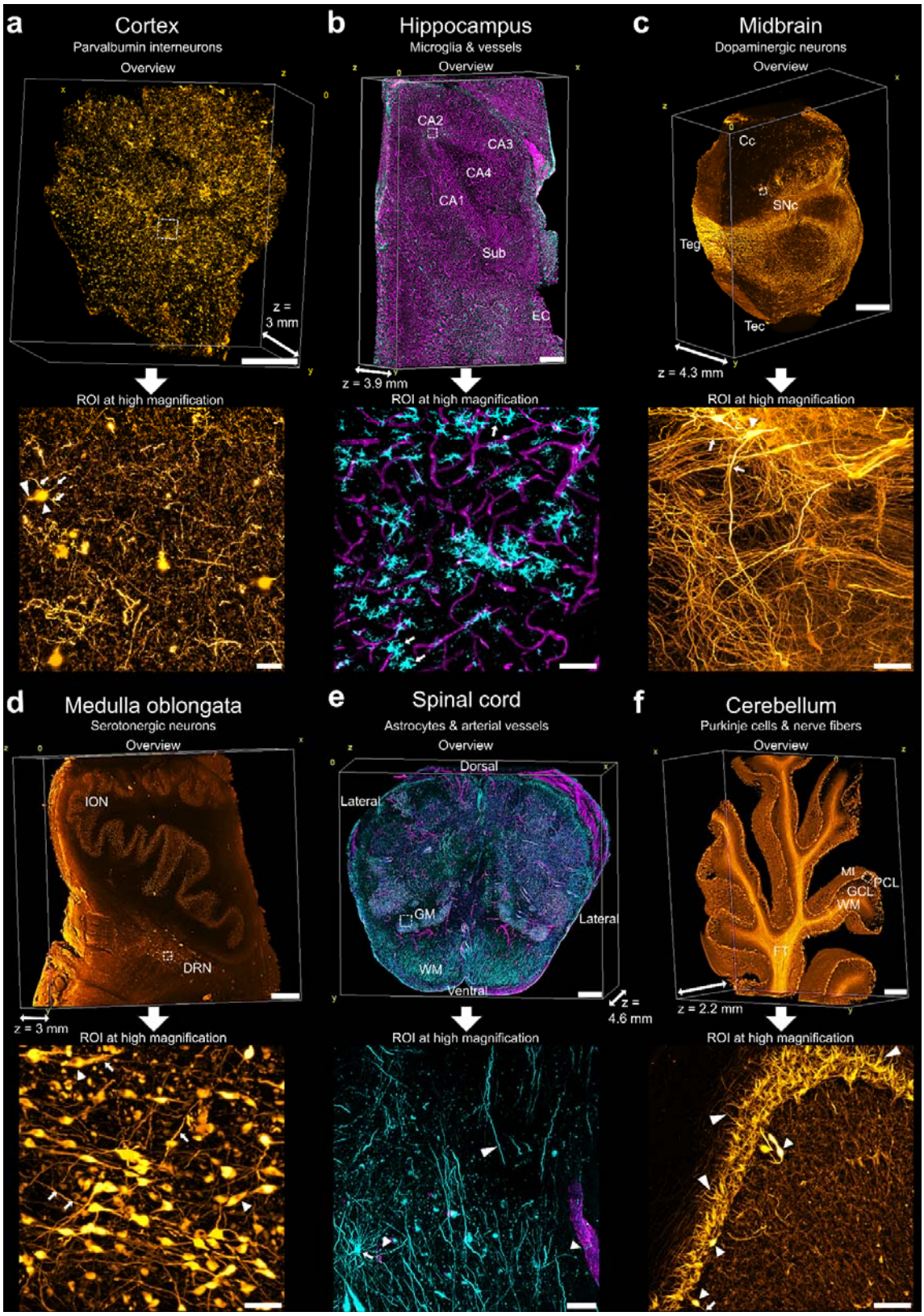


**Figure 2. 3D histology of different human CNS regions.** For each panel, 3D rendering of a whole-mount imaged sample (top; imaged at 0.8x-2x magnification) is shown together with a region-of-interest (ROI; bottom) imaged at higher magnification (12.6x), using mesoSPIM V5. The ROIs are indicated in the rendering by dashed white boxes. **a**, Parvalbumin-positive interneurons in archival human cortex. Scale bar: 1 mm. The ROI reveals neuronal somata (small arrowhead) with axons (large arrowhead) and dendrites (arrows). Scale bar: 100 µm. **b**, IBA1-positive microglia (cyan) and

podocalyxin-positive blood vessels (magenta) in aged archival human hippocampus across distinct anatomical subregions (cornu ammonis (CA)4, CA3, CA2, CA1, subiculum (Sub), and entorhinal cortex (EC)). Scale bar: 1 mm. The ROI reveals microglia morphology with their short processes (arrows) close or attached to blood vessels. Scale bar: 50 µm. **c**, Tyrosine hydroxylase (TH)-positive dopaminergic neurons in archival human midbrain, with the crus cerebri (Cc), tegmentum (Teg), tectum (Tec), and substantia nigra pars compacta (SNc). Scale bar: 2 mm. The ROI highlights large dopaminergic neurons with somata (arrowhead) and long neurites (arrows), branching into a dense fiber network. Scale bar: 50 µm. **d**, Tryptophan hydroxylase (TPH)2-positive serotonergic neurons in archival human medulla oblongata. Distinct lower brainstem nuclei such as the inferior olivary nucleus (ION) and the dorsal raphe nucleus (DRN) are visible. Scale bar: 1 mm. The ROI displays serotonergic neurons with nuclei (arrowheads) and widely ramified neurites (arrows). Scale bar: 50 µm. **e**, GFAP-positive astrocytes (cyan) and SMA-positive arterial vessels (magenta) in archival human spinal cord. The characteristic butterfly-like shape of the grey matter (GM) can be distinguished from the white matter (WM) due to distinct astrocytic staining patterns. Scale bar: 1 mm. The ROI displays stellate astrocytes (arrow) and long glial processes (large arrowhead) besides arterial vessels (small arrowheads). Scale bar: 50 µm. **f**, Archival human cerebellum, stained with anti-neurofilament antibody. Cerebellar anatomy with fiber tracts (FT) of the WM and distinct cortical layers, consisting of the molecular layer (ML), Purkinje cell layer (PCL), and granular cell layer (GCL). Scale bar: 1 mm. The ROI displays Purkinje cells with somata (small arrowheads), arborized dendrites (large arrowheads), and axons (arrow). Scale bar: 50 µm.

### *3D histology of human organs beyond the CNS*

In principle, aDISCO should be applicable to human organs other than the CNS, but adaptations may be needed because of differences in tissue composition. We therefore processed whole-mount FFPE human tissue blocks from disparate organs, stained them with a panel of antibodies, and imaged them by light-sheet microscopy (Fig. 3, Suppl. Videos 4, 5). With aDISCO, we visualized myelinated fibers in peripheral nerve, myelinated and unmyelinated nerve fibers in the skin, skeletal muscle fibers together with their vascularization, cardiac myocytes and arteries in the heart, glomeruli and tubules in the kidney, sinusoids in the spleen, bile ducts in the liver, bronchioles and alveoli in the lung, and mucosa with crypts in the colon.

These examples demonstrate that aDISCO achieves effective clearing and immunolabeling of cellular structures across a broad variety of human organs. This finding was supported by MFI projections, which showed robust staining signals throughout the various human organs (Extended Data Fig. 4). This was also true for very dense tissues, such as liver or skin. Again, imaging depth was not limited by the quality of clearing but by the size of the respective tissue blocks, which was 10.7 ± 4.7 mm (mean ± s.d. across n = 9 samples) x 7.6 ± 3.2 mm, and 4.3 ± 1.5 mm thick, with a maximal sample thickness of 6.5 mm (lung sample).

The clearing and staining quality enabled the resolution of thin structures (insets in Fig. 3), including the branches of sensory nerve terminals in the epidermis of the skin (inset in Fig. 3b) and the Bowman capsules and outgoing proximal tubules of glomeruli in the kidney (inset in Fig. 3e).

In conclusion, our findings highlight the versatility of aDISCO for 3D histology of whole-mount FFPE human tissue blocks across multiple organs and its compatibility with a broad range of antibodies for detailed organ characterization.

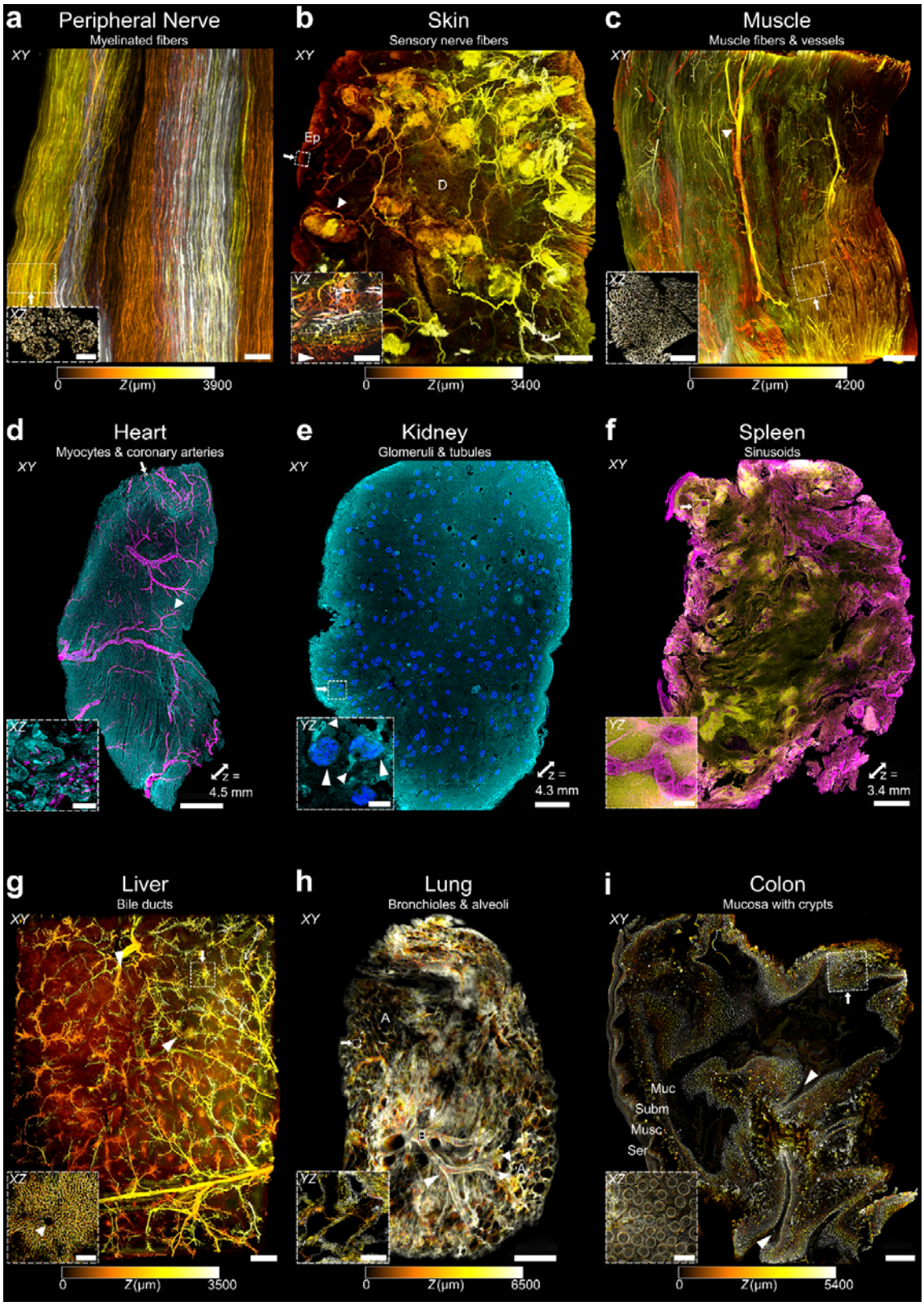

**Figure 3**. **3D histology of human organs beyond the CNS.** Each panel displays an xy-projection for sample overview, imaged at 0.63x-12.6x magnification using mesoSPIM V5. Panels a-c and g-i are depth color-encoded to show the three dimensions of each sample. Panels d-f are maximum-intensity projections with indicated z-thickness of each sample to illustrate double antibody staining. The insets in each panel (bottom left) display orthogonal sections each of a region-of-interest (ROI) from the same sample imaged at higher magnification (4x-20x using mesoSPIM V5 and V6) to demonstrate high axial resolution in z. The ROIs are indicated in the depth color-encoded overview by dashed white boxes and the direction of the ROI viewport is illustrated by the arrow next to the white box. **a**, MBP-positive myelinated fibers in archival human peripheral nerve. The longitudinal view displays the cotton wool-like pattern of thin nerve fibers. Scale bar: 500 µm. The inset highlights nerve fascicles composed of individual myelinated fibers in the transversal view. Scale bar: 100 µm. **b**, PGP9.5-positive sensory nerve fibers in archival human skin. The longitudinal view displays branching nerve fibers in the epidermis (Ep) and dermis (D), forming Pacinian corpuscles (small arrowhead). Scale bar: 1 mm. The inset highlights the innervation pattern of the epidermis by thin sensory nerve terminals (large arrowhead). Scale bar: 100 µm. **c**, Laminin-positive muscle fibers and blood vessels in archival human skeletal muscle with prominent vascularization (arrowhead in the longitudinal view). Scale bar: 1 mm. The inset highlights muscle fascicles composed of individual muscle fibers in the transversal view. Scale bar: 200 µm. **d**, N-cadherin-positive myocytes (cyan) and SMA-positive coronary arteries (magenta) in archival human heart. The longitudinal view highlights branching of coronary arteries (arrowhead) in the myocardium. Scale bar: 2 mm. The inset displays a ROI xz-projection at high magnification and shows smaller arterioles between myocytes. Scale bar: 30 µm. **e**, Nephrin-positive glomeruli and E-cadherin-positive tubules in archival human kidney. Scale bar: 1 mm. The inset displays a ROI yz-projection at high magnification with detailed morphology of glomeruli with Bowman capsules (large arrowheads) and outgoing proximal tubules (small arrowheads). Scale bar: 150 µm. **f**, SMA-positive sinusoids in CD45-positive lymphatic tissue of archival human spleen. Scale bar: 1 mm. Inset scale bar: 100 µm. **g**, CK19-positive bile ducts in archival human liver, displaying the branching pattern (large arrowheads) of hepatic bile ducts in the longitudinal view. Scale bar: 1 mm. The inset shows a hepatic lobule with central vein (small arrowhead) surrounded by bile ducts in the transversal view. Scale bar: 200 µm. **h**, CK7-positive airways in archival human lung. In the longitudinal view, the bronchiolar tree with bronchioles (B), branching (large arrowhead) and segueing (small arrowheads) into peripheral alveoli (A) is visible. Scale bar: 2 mm. The inset displays a ROI yz-projection of alveoli. Scale bar: 100 µm. **i**, Collagen-IV-positive human colon sample. The longitudinal view highlights deeply caved mucosal crypts (arrowheads) within the colon wall composed of mucosa (Muc), submucosa (Subm), muscularis (Musc), and serosa (Ser). Scale bar: 1 mm. The inset shows the arrangement of individual crypts within the colon wall structure from the inner mucosa to the outer serosa (double arrow) in the transversal view. Scale bar: 300 µm.

### *3D cortical profiling of neuronal density in archival human brain*

Since cleared samples can be imaged volumetrically using 3D microscopy, aDISCO may enable the three-dimensional quantitative morphometry of tissue such as human cortex with analytical precision that is unattainable by conventional histology. The human cortex exhibits a characteristic architecture consisting of six neuronal layers[36] and is essential for performing complex neuronal computations, which are the basis of cognition and behavior. Precise quantification of cortical neurons and their distribution across distinct layers may help advance the understanding of the relationships between functional integrity and cellular organization in the human cortex. This knowledge may be relevant to many fields of neuroscience, from refining models of neuronal computation to elucidating structural alterations during development, aging, and in pathological states.

The characterization of human cortical layers[37] relies primarily on 4-5 µm thin 2D sections[38, 39]. In contrast, comprehensive examination of large human cortical specimens in 3D has been limited to counting the total cell number via staining with small molecular dyes which cannot differentiate between neurons and other cell types[16, 17]. In this study, specific immunolabeling of neurons with anti-NeuN antibody allowed us to precisely assess neuronal

density in large archival human cortex specimens, enabling detailed three-dimensional profiling of the neuronal density across cortical layers (Fig. 4).

We devised a 3D data analysis pipeline for efficient and accurate neuron counting in large datasets (Fig. 4b-c). We used ILASTIK[40] and ClearMap[41] for segmentation and detection of neuronal cell candidates, which were subsequently refined by merging falsely separated parts of neurons. Candidates were then classified as cells vs. non-cells using a supervised deep convolutional neural network (DCNN) that used three orthogonal virtual slices of the local environment of the neuronal cell candidate to predict its class (cross-validated accuracy 92.2%; Extended Data Fig. 5).

This approach enabled robust detection of neurons and subsequent determination of neuronal density in human cortex (Fig. 4d-f, Suppl. Video 6). To define cortical layers, we used visual guidance to annotate landmarks that indicate specific layers or boundaries between layers and fitted them to polynomial hyperplanes, enabling precise determination of neuronal densities across cortical layers (Fig. 4g-h). To compensate for variable cortical thickness within a 3D sample, we normalized layer thickness by the average distance between landmarks. As a result, we obtained a layer-dependent neuronal density profile which can distinguish cortical layers, except layers 5 and 6, where the transition is also morphologically less well-defined (Fig. 4i).

In summary, our analyses show that large archival human samples processed via aDISCO provide clearing and antibody staining quality that is amenable to segmentation and object detection. Our 3D data analysis pipeline allows for accurate detection of neurons and delineation of neuronal densities across cortical layers in three spatial dimensions. By establishing a reference profile of neuronal cell distribution in normal human cortex, we provide a basis for assessing cortical abnormalities under pathological conditions.

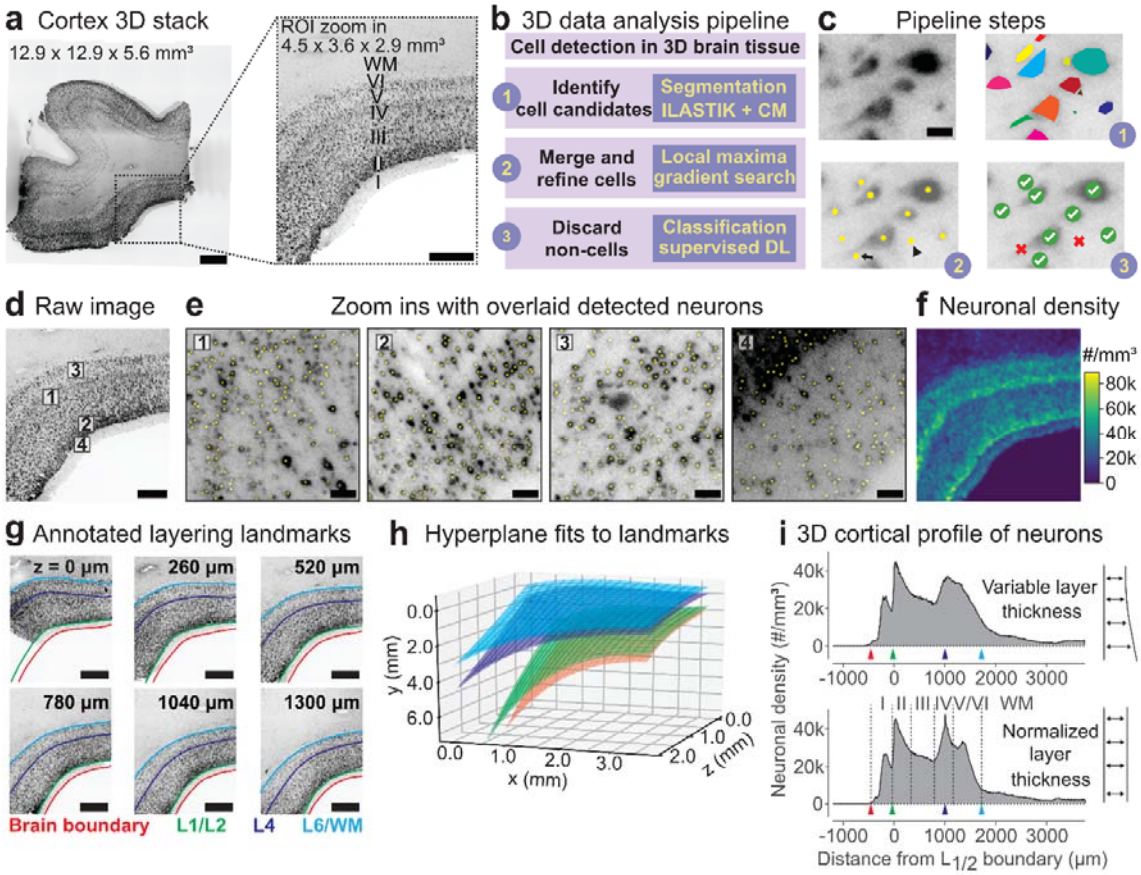


**Figure 4. Determination of neuronal density in archival human brain cortex. a**, Left: Stitched and 4x-downsampled 3D stack of FFPE human cortex specimen, stained for neurons with anti-NeuN antibody and imaged at 4x magnification using mesoSPIM V5. Scale bar: 2 mm. Right: Digital zoom into a region-of-interest (ROI) to highlight cortical layers I-VI and white matter (WM). Scale bar: 1 mm. **b**, 3D data analysis workflow for neuronal cell detection in three steps. CM: ClearMap, DL: deep-learning. **c**, Illustration of the pipeline steps explained in (b). Upper left: Raw fluorescence image. Scale bar: 20 µm. Upper right: Segmented neuronal cell candidates, visualized by different colors. Lower left: Detection of cortical neurons based on local maxima (yellow dots) of segmented neuronal cell candidates. Note false positive detection of axons separated from somata (arrow) and of noise (arrowhead). Lower right: Falsely detected cell candidates are discarded (red crosses) via supervised DL, while correctly detected neurons are kept (green check marks). **d**, Raw fluorescence image of cortical layers. Scale bar: 1 mm. **e**, Digital zoom-in micrographs of regions numbered in (d) with overlaid detected neurons (yellow dots). Scale bars: 50 µm. **f**, Spatial mapping of neuronal density. #: neuron count. **g**, 3D annotation of visually identified layering landmarks for defining distinct layers (L), indicated by the different colors and exemplarily shown along the z-axis. Scale bars: 1 mm. **h**, Generation of polynomial hyperplanes fitted to the respective layering landmarks. **i**, Neuronal density per $mm^3$ across all cortical layers, defined by the landmark hyperplanes in (h) as indicated by the colored arrowheads and plotted according to the distance from the boundary between layers 1 and 2 (L1/2). 3D cortical profile before (upper histogram) and after normalization to variable layer thickness (lower histogram).

### *3D histological investigation of focal cortical dysplasia (FCD)*

To test a use case for these new tools, we investigated the cortical architecture in a neurodevelopmental disorder. FCD is a neurodevelopmental malformation disorder causing pharmaco-resistant epilepsy in children and young adults[42]. Its prevalence within the general population is < 1%[43], but ranges between 5% to 25% among patients suffering from focal epilepsy[44]. FCD is characterized by distortions in cortical layer architecture and is classified

in three different types depending on the histopathological phenotype[45, 46]. Type I is characterized by isolated abnormal radial and/or tangential cortical lamination. Type II is the most prevalent and characterized by dysmorphic neurons (subtype IIa) or additionally "balloon cells" (subtype IIb), which may represent non-functional neural progenitor cells with enlarged cell bodies. Type III is associated with other pathologies such as hippocampal sclerosis, neoplasia, or vascular malformations. Ectopic neurons within the white matter can be found in all FCD types.

The diagnostic assessment of FCD in thin 2D histological sections suffers from inherent limitations. Firstly, the inherent focal nature of FCD makes it difficult to identify pathological foci in large surgical specimens obtained from complete epileptic zone excision[47-49]. This requires exhaustive and time-consuming serial sectioning. Secondly, suboptimal brain tissue orientation during FFPE block embedding and sectioning may impede accurate evaluation of cortical layering, which is crucial for FCD diagnosis. Lastly, FCD can manifest multifocally[42], rendering single thin sections inadequate for portraying the full pathological spectrum. The latter consideration is pivotal for estimating disease severity and devising appropriate follow-up interventions. Therefore, we were curious to assess if 3D histology could help improve FCD diagnostics in difficult cases and accurately assess the extent of pathology in the entire surgical specimen. The compatibility of aDISCO with FFPE specimens from diagnostic archives allowed us to retrieve adequate numbers of historical specimens and benchmark 3D histology against traditional analyses.

We selected 7 FCD cases confirmed by 2D histology from the diagnostic archive of the University Hospital of Zurich (Extended Data Table 2). All patients had undergone surgery due to refractory epilepsy. Only in three cases could the pathology be assessed with conventional histology throughout all cortical layers due to the limitations of 2D histology. For control, we selected 7 autopsy samples of patients with normal histology in the respective cerebral lobes from the diagnostic archive of the University Hospital of Zurich.

We stained neurons with anti-NeuN antibody to assess neuronal density across all cortical layers for 3D cortical profiling. Qualitative inspection of 3D stacks revealed focal distortion of the typical cortical layer architecture (cf. Fig. 4a), with only the molecular layer (I), the external granular layer (II), and the beginning of the white matter (WM) distinguishable, but not the layers in between (Fig. 5a, b). Furthermore, we observed ectopic neurons in the white matter. In contrast to the reference profile of normal cortex (cf. Fig. 4i), the cortical neuronal density profile in FCD exhibited only two peaks for layers I and II, while the other layers merged into a single hill that flattened slowly towards the white matter (Fig. 5c). This analysis demonstrates that 3D cortical profiling of neuronal density reflects the distortion of cortical layer architecture in FCD.

To investigate an additional hallmark of FCD, we quantified the volume of cells. This analysis identified correctly the characteristic large and round balloon cells of FCD type IIb (Fig. 5d-e).

Furthermore, during visual inspection of 3D stacks from FCD patients, we noticed multiple foci of neuronal loss, substantially varying in size and shape within and between patients (Fig. 5f). Based on the clinical history of FCD patients, these lesions were not caused by electrode implantations for two reasons: First, some patients who exhibited lesional foci had not undergone any electrode implantations. Second, for those who had been implanted with electrodes, the lesional foci did not match the electrode pattern in size and shape.

To analyze the extent of focal neuronal loss, we annotated all lesions in the entire 3D stacks (Fig. 5g). Quantification revealed that only 2.2% of the cortical volume of all FCD samples was affected (Fig. 5h; Extended Data Table 3). When we analyzed the 3D stacks as optical xy-sections along the z-axis, foci of neuronal loss were detected in less than half of optical sections (Fig. 5i). Most lesional foci were small and the maximally affected area per optical slice was 20%. Hence, the chance of missing such foci in thin sections, as in conventional 2D diagnostics, is high.

Finally, we quantified the overall neuronal density in brain volumes, including the lesional foci and the surrounding inconspicuous brain tissue in FCD (Fig. 5j, k). Bivariate analysis showed a strong negative correlation between overall neuronal density and the extent of lesional foci in FCD patients, indicating that FCD specimens with a higher fraction of brain volume with focal loss also exhibited overall lower neuronal density (Fig. 5l). Comparison between FCD and control group revealed a significant reduction of neuronal density in FCD patients (median reduction of 43%; Fig. 5m, Extended Data Table 3). Thus, the overall neuronal loss in FCD (43%; Fig. 5m) exceeded the loss caused by lesional foci (2.2% of cortical volume; Fig. 5h) and affected brain tissue that would have been classified as healthy by conventional histology, revealing additional neuronal loss undetectable by visual inspection. In summary, our analyses demonstrate that aDISCO can be used to address specific pathologies by quantitative and comprehensive 3D histology, facilitated by a largely automated 3D data analysis pipeline.

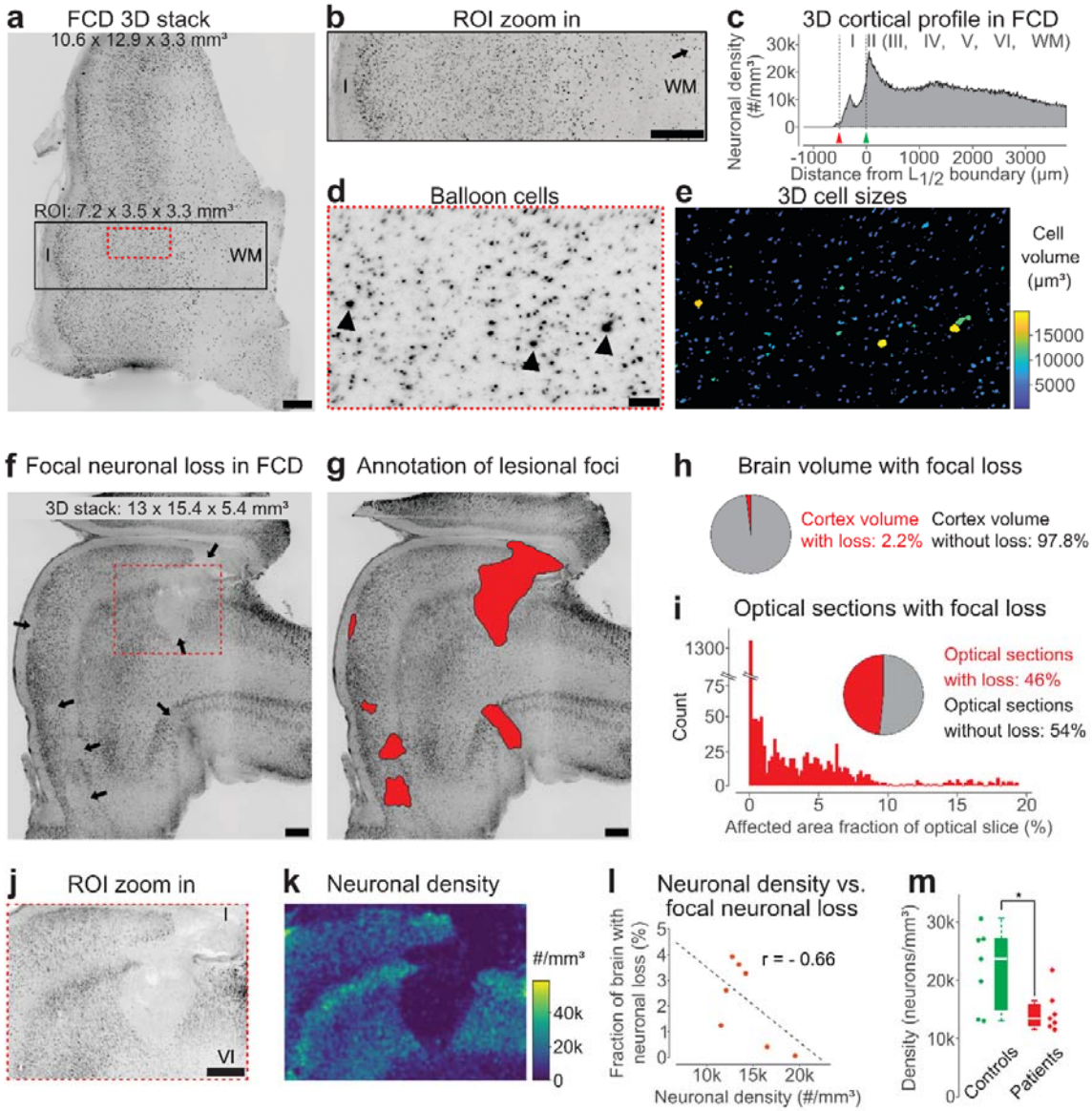


**Figure 5. 3D histological examination of FCD. a,** Stitched and 4x-downsampled 3D stack of archival human FCD cortex imaged at 4x magnification using mesoSPIM V5. Distortion of layer architecture from the molecular layer (I) to the white matter (WM) is visible. Scale bar: 1 mm. **b**, Region-of-interest (ROI) digital zoom into the black-lined box, highlighting distortion of cortical layer architecture and ectopic neurons in the WM (arrow). Scale bar: 1 mm. **c**, Neuronal density profiling in FCD, displayed as number (#) of neurons per $mm^3$ across all cortical layers, defined by the distance to the L1/2 boundary. Only two peaks, corresponding to layers I and II, can be distinguished from an otherwise undifferentiated hill which flattens into the WM. **d**, ROI digital zoom into the red-dashed box, highlighting large and round balloon cells (arrowheads). Scale bar: 200 µm. **e**, Automated detection of balloon cells based on their large cell size (yellow). Color scale indicates range of cell volume in $µm^3$. **f**, Stitched and 4x-downsampled 3D stack of archival human FCD cortex imaged at 4x magnification using mesoSPIM V5. Multiple foci of neuronal loss (arrows) can be identified. Scale bar: 1 mm. **g**, Illustration of 3D annotation of lesional foci (red). Scale bar: 1 mm. **h**, Quantification of lesional foci in entire brain tissue blocks. **i**, Quantification of lesional foci in optical sections. The histogram displays the count of optical sections in relation to the affected area per optical slice. **j**, ROI digital zoom into the red-dashed box, highlighting a large focus of neuronal loss which affects all cortical layers I-VI. Scale bar: 500 µm. **k**, Quantification of overall neuronal density in the lesional focus and the surrounding inconspicuous brain tissue, displayed as number (#) of neurons per $mm^3$ in a heatmap. Color scale indicates cell number range in thousands (k). **l**, Correlation of focal neuronal loss in percentage (%) and overall neuronal density displayed as number (#) of neurons in thousands (k) per $mm^3$. Correlation coefficient r = -0.66. **m**, Comparison of quantified overall neuronal density in FCD patients (red; n = 7) and controls (green; n = 7), displayed as number of neurons in thousands (k) per $mm^3$ in box plots. Statistical analysis was performed by two-sided Student's t-test. *p = 0.026.

## Discussion

Here, we introduce aDISCO, a method for 3D histology of whole-mount FFPE human tissue blocks, as a complementary diagnostic technique to conventional microscopy. We demonstrate that aDISCO achieves effective clearing and antibody staining throughout entire archival tissue blocks from different human organs and is compatible with a variety of antibodies, enabling specific immunolabeling of target structures down to the cellular level.

A central feature of aDISCO is the consistent clearing and homogeneous antibody staining of whole-mount FFPE human tissue blocks, whose sizes surpass the state-of-the-art for human FFPE specimens[14, 19, 26, 28] (Extended Data Table 1). Imaging such large samples at cellular resolution with high throughput has only recently become a widely used approach due to the development of light-sheet microscopes with large working-distances[29, 30, 50]. The largest human samples cleared and stained to date were freshly processed with the SHANEL protocol[17, 18]. In this organic solvent-based tissue clearing method, the blood vessels of the respective human organs were perfused with chemical reagents to circumvent the diffusion barrier. With this procedure, a maximal imaging depth of 1 cm was reached for antibody-stained tissue. However, this approach is not applicable to archival human FFPE specimens from diagnostic archives. The greatest imaging depth in FFPE tissue so far had been achieved with the organic solvent-based DIPCO protocol[14]. However, DIPCO was applied to short-term formalin-fixed paraffin-embedded human biopsies (usually fixed < 24 hours) as opposed to long-term formalin-fixed paraffin-embedded human tissue specimens from autopsy (usually fixed > 24 hours up to three weeks, depending on organ type and size). In the DIPCO study, a maximal imaging depth of 1.6 mm was reached in human tumor biopsy specimens from six different human organs, characterized with five antibodies. To date, the only human tissue clearing method performed on long-term formalin-fixed and paraffin-embedded human autopsy tissue was OPTIClear[19]. With a combination of organic solvents used for deparaffination and a CLARITY-related clearing approach, this method reached a maximal imaging depth of 546 µm for antibody staining in human brain tissue. In contrast, in our study we reached an imaging depth of 6.5 mm, with the sizes of the available samples being the limiting factor for the maximum imaging depth. Archival human FFPE tissue samples that were homogeneously cleared and immuno-stained in our study reached a maximal size of 18.5 × 11.9 × 6.5 $mm^3$ (lung sample) after clearing-induced tissue shrinkage. The average sample thickness was 4.1 ± 1.0 mm (mean ± s.d. across 16 samples; lateral extent 9.8 ± 4.2 mm for the long and 7.6 ± 2.6 mm for the short side). Thus, with aDISCO we have established a human tissue clearing method which enables access to whole-mount archival human tissue blocks by being compatible with both large human tissue specimens and samples from long-term FFPE storage (up to 15 years old in our study).

A second unique feature of aDISCO is its tested compatibility with 11 different human organs. This broad range of applications surpasses all existing clearing methods to date. Previous

human tissue clearing methods were typically performed on one or a few tissue types (Extended Data Table 1). Most studies focused on human brain cortex[13, 15, 17, 19, 20, 22-27], which is relatively straightforward to render transparent. In contrast, reports on dense tissues such as liver or skin, which are more challenging to clear[9, 31], are sparse. In human skin, previous work achieved a maximum imaging depth of 300 µm in immunolabeled tissue, while a depth of 1.4 mm was reached in unstained, autofluorescent tissue[51, 52]. Similarly, in human liver most studies reached imaging depths of only a few hundred micrometers for antibody staining[53-56]. Notably, only two studies successfully imaged human liver volumes of 2.5 mm and 3 mm thickness, respectively[57, 58]. However, human tissue clearing of archival FFPE skin or liver tissue had not been previously performed. With aDISCO, we achieved imaging depths of 3.4 mm in immunolabeled archival human skin and 3.5 mm in immunolabeled archival human liver tissue, values that again were only limited by the thickness of the available whole-mount FFPE blocks.

The third key advantage of aDISCO is its compatibility with at least 22 commonly used antibodies for cell typing, surpassing previous human tissue clearing studies. Antibody compatibility has been a significant challenge in tissue clearing and prior testing of antibodies with the specific chemicals and conditions used in clearing protocols has therefore been recommended[10, 59]. Most antibodies were so far tested for compatibility only in non-archival human tissue[17, 18, 25, 27] (Extended Data Table 1). The study with the largest FFPE human tissue specimens (3 mm thick after clearing-induced tissue shrinkage) to date used staining with low-molecular-weight dyes[16], which, compared to antibodies, diffuse more easily into thick tissues but lack the ability to differentiate distinct cell types. aDISCO overcomes these limitations, providing compatibility with diverse antibodies and consistent immunolabeling throughout whole-mount archival human tissue blocks.

As aDISCO was found to be compatible with large archival tissue samples from many different human organs and antibodies, it can be applied to a broad range of archival tissues and allows for distinct characterization of target structures by specific immunolabeling. The option for reparaffination highlights the protocol's versatility for subsequent conventional 2D histology after tissue clearing.

Finally, we show in a use-case study that aDISCO can be applied for standardized 3D histology of collected human samples from the diagnostic archive to investigate biological and pathological questions. In previous tissue clearing studies aiming to examine large human cortex specimens in 3D, staining was performed not with antibodies but with dyes that label all cells irrespective of distinct cell types[16, 17]. Therefore, specific 3D quantification of neuron counts in large human cortex samples had not been performed to date. Here, we demonstrate how aDISCO enabled the quantification of neuronal density and the assessment of cortical layer profiles via specific immunolabeling of neurons and a largely automated data analysis pipeline.

We investigated a case series of focal cortical dysplasia (FCD), a neurodevelopmental malformation disorder, whose focal and subtle pathology can be overlooked during diagnostic assessment by conventional 2D histology. 3D cortical profiling reflected the distortion of cortical layer architecture in FCD. Furthermore, cell volume analysis correctly identified large and round balloon cells, which are characteristic of the most prevalent FCD subtype IIb and whose detection therefore helps in FCD diagnosis. Together, these advancements may improve diagnostic assessment of FCD, particularly in cases with mild or borderline features. Moreover, we detected multiple foci of neuronal loss in FCD cortex. This neuronal loss may be the consequence of the long-lasting epilepsy and the lesional foci may correspond to excitotoxic damage in overactive neuronal ensembles.

Previously, only two studies have reported neuronal loss in FCD using conventional 2D histology[60, 61]. However, the extent of neuronal loss in the entire affected cortex had not been determined to date. aDISCO-based 3D histology showed that only a minor fraction of the cortical volume in whole-mount FFPE tissue blocks was affected by the lesional foci, yet there was additional neuronal loss not visible by eye and only detectable via quantification of cell densities. Together, these findings underscore the importance of 3D histology for holistic examination of human tissue specimens and promise to entail direct implications for diagnostic quality in FCD.

In conclusion, aDISCO marks a significant advancement in human tissue clearing, enabling organ- and cell type-specific 3D histology of archival whole-mount human tissue blocks previously inaccessible due to long-term FFPE storage. Diagnostic archives contain large numbers of human samples from the distant past and thus constitute an untapped potential to study specific and rare diseases. Therefore, aDISCO provides a versatile method for 3D histology that can process whole-mount FFPE human tissue blocks collected over years to decades. In summary, aDISCO's broad applicability, compatibility with diverse antibodies, and integration with automated 3D data analysis can contribute to improved histological diagnostics and deeper insights into human diseases.

## Materials and Methods

### *Archival human FFPE samples*

All procedures and the associated guidelines for processing archival FFPE human tissue were approved by the cantonal ethics committee Zurich (BASEC-No. 2022-00293). FFPE human tissue blocks were selected from the surgical and autopsy diagnostic archive at the Institute of Neuropathology and the Institute of Pathology and Molecular Pathology, University Hospital Zurich. The samples for testing compatibility of the aDISCO protocol with CNS regions and human organs originated from autopsies and were selected in a pseudonymized way. For the use-case study, FFPE brain surgical specimens from 7 FCD patients were chosen from the diagnostic archive. Patients with FCD were selected based on available clinical data and neuropathological diagnosis from conventional 2D histology. The hospital software database “KISIM” was used to check the medical history of FCD patients. Autopsy samples from 7 patients with normal histology in the respective cerebral lobes served as controls. For controls, only basic demographic information and brain location were available due to pseudonymization of control FFPE tissue blocks. Exclusion criteria for controls encompassed any pathologies in the respective brain region.

### *Deparaffination of whole-mount archival human tissue blocks*

FFPE human tissue blocks were melted for 1 hour at 60°C in a tissue embedding system TES99 (Medite). Samples were transferred into glass vials with closed top cap (C226-0020, Thermo Fisher Scientific). The remaining wax was removed by incubation in xylene (253-VL51TE, Thommen-Furler AG) 2 times each for 1 hour at 37°C, shaking at 50 rpm. Samples were rehydrated in decreasing serial solutions (100%, 95%, 90%, 80%, 70%, 50%, 25%) of ethanol (20821.321, VWR Chemicals) in Milli-Q® water (Merck Millipore) each for 1 hour at room temperature, shaking at 50 rpm, and finally in 1x PBS overnight at room temperature, shaking at 50 rpm.

### *Dehydration and pre-clearing*

Samples were dehydrated in increasing serial solutions (20%, 40%, 60%, 80%) of THF (186562, Sigma Aldrich) in Milli-Q® water each for 1 hour at room temperature, shaking at 50 rpm, followed by 2 times 100% THF each for 1 hour at room temperature, shaking at 50 rpm. Pre-clearing was performed in a 2:1 solution of DCM (270997, Sigma Aldrich) to THF overnight at room temperature, shaking at 50 rpm.

### *Rehydration and bleaching*

DCM was washed out by incubating the samples 2 times in 100% THF each for 30 minutes at room temperature, shaking at 50 rpm. Rehydration was achieved in decreasing serial solutions (80%, 60%, 40%) of THF in Milli-Q® water each for 1 hour at room temperature, shaking at 50 rpm. To pre-cool the samples for bleaching, the rehydration step in 20% THF in Milli-Q® water was performed for 1 hour at 4°C, shaking at 50 rpm. Bleaching was conducted in 28% $H_2O_2$ (1.08600.2500, Merck Millipore) with 4% THF in Milli-Q® water for 20 hours at 4°C in the dark, shaking at 50 rpm.

### *Autofluorescence removal*

To wash out the bleaching solution, samples were incubated 2 times in 1x PBS each for 1 hour at room temperature, shaking at 50 rpm. To remove remaining autofluorescence from highly pigmented samples, tissue blocks were incubated in 10 mM cupric sulfate (61230, Fluka) in 50 mM ammonium acetate (A-7330, Sigma Aldrich) buffer in Milli-Q® water, pH = 5, for 3 hours at room temperature in the dark, shaking at 50 rpm. The solution was washed out by subsequent incubation in 1x PBS 2 times each for 1 hour, and then overnight at room temperature, shaking at 50 rpm.

### *Antigen retrieval*

Depending on the respective antibodies, antigen retrieval was achieved by treating the samples with 10-30% formic acid (4724.3, Roth) solution in Milli-Q® water, pH = 2, for 3 hours at room temperature, shaking at 50 rpm. The solution was washed out by incubation in 1x PBS for 1 hour at room temperature, shaking at 50 rpm.

### *Permeabilization and decolorization*

Samples were first permeabilized with 0.2% TritonX-100 (X100, Sigma Aldrich) in 1x PBS 2 times each for 1 hour at room temperature, shaking at 50 rpm. Stronger permeabilization and decolorization was achieved by subsequent incubation in 25% urea (U4884, Sigma Aldrich) + 25% NNNN-tetrakis(2-OH-propyl)ethylenediamine (122262, Sigma Aldrich) + 15% TritonX-100 in 1x PBS overnight at 37°C, shaking at 50 rpm. Permeabilization was continued in 0.2 % TritonX-100 + 2.3% glycine (G8898, Sigma Aldrich) + 20% DMSO (D8418, Sigma Aldrich) + 0.5 mM methyl-beta-cyclodextrin (332615, Sigma Aldrich) + 0.2% trans-1-acetyl-4-OH-$_L$-proline (441562, Sigma Aldrich) + 0.1% sodium azide (S8032, Sigma Aldrich) in 1x PBS for 3 days at 37°C, shaking at 50 rpm.

### *Blocking and staining*

For blocking and staining, samples were transferred from glass vials into 6- (92006, TPP) or 12-well plates (92012, TPP), depending on sample size, and sealed with parafilm (10018130, Bemis) during incubation to avoid evaporation. Blocking was performed in 0.2% Tween-20 (P2287, Sigma Aldrich) + 0.1% heparin (10 mg/ml, 2835358, B. Braun Medical AG) + 5% DMSO + 6% donkey serum (017-000-121, Jackson Immuno Research) in 1x PBS for 2 days at 37°C, shaking at 50 rpm. Staining was conducted in 0.2% Tween-20 + 0.1% heparin (10 mg/ml) + 5% DMSO + 0.1% sodium azide (staining buffer) for up to 4 weeks, depending on the sample size and antibody diffusion capacity, at 37°C, shaking at 50 rpm. To enhance the diffusion capacity of antibodies, staining was carried out gradually, starting with low antibody concentration and adding more and more antibodies to the staining solution to finally reach the calculated final antibody concentration at the end of the staining time. For this gradual staining step, the starting and final antibody concentrations as well as the staining times were adapted to the specific antibodies used in this study (Suppl. Table 1). For example, when the final dilution of an antibody with a stock concentration of 1.5 mg/ml was 1:200 and the staining time was two weeks, we started with a dilution of 1:800 and added the same dilution another three times every half a week, thus reaching the final dilution of 1:200 after two weeks.

Between primary and secondary antibody staining, samples were washed in staining buffer 2 times each for 1 hour, then 2 times each for 2 hours, and then overnight at room temperature, shaking at 50 rpm. After secondary antibody incubation, samples were washed in staining buffer 2 times each for 1 hour, then 2 times each for 2 hours, and then for 2 days at room temperature, shaking at 50 rpm.

### *Dehydration and clearing*

Samples were dehydrated in increasing serial solutions (20%, 40%, 60%, 80%) of THF in Milli-Q® water each for 1 hour at room temperature, shaking at 50 rpm, followed by 2 times 100% THF each for 1 hour at room temperature, shaking at 50 rpm. Final delipidation was performed in a 2:1 solution of DCM to THF overnight at room temperature, shaking at 50 rpm, followed by incubation in 100% DCM 2 times each for 2 hours at room temperature, shaking at 50 rpm. Refractive index ($n_D$ = 1.56) matching was achieved in DBE (108014, Sigma Aldrich) overnight at room temperature, non-shaking.

### *Reparaffination of cleared tissue blocks*

DBE was washed out by incubating the tissue blocks in 100% methanol (203-VL03K-/1, Thommen-Furler AG) 2 times each for 1 hour at room temperature, shaking at 50 rpm. Samples were rehydrated in decreasing serial solutions (80%, 60%, 40%, 20%) of methanol

in Milli-Q® water each for 1 hour at room temperature, shaking at 50 rpm, followed by incubation in 1x PBS overnight at room temperature, shaking at 50 rpm. Tissue blocks were again dehydrated in increasing serial solutions (25%, 50%, 70%) of ethanol in Milli-Q® water each for 1 hour at room temperature, shaking at 50 rpm. Then, samples were put in the Leica ASP300S Fully Enclosed Tissue Processor (Leica Biosystems) and the following program started: 100% ethanol for 45 minutes, 1 hour, and 30 minutes at 37°C, followed by 100% ethanol 2 times each for 1 hour at 45°C; then xylene for 45 minutes and 2 times each for 1 hour at 37°C; and finally paraffin (39601006, Leica Biosystems) for 1 hour and 15 minutes, 1 hour and 30 minutes, and 2 hours at 62°C.

### *2D histology*

2-µm thick tissue sections were cut from the tissue blocks, using a semi-automated rotary microtome, (RM2245, Leica Biosystems) and mounted onto slides (0810531, HistoBond®). Slides were deparaffinized by incubation in xylene 2 times each for 10 minutes at room temperature. Slides were rehydrated in decreasing serial solutions (100%, 95%, 90%, 80%, 70%) of ethanol in Milli-Q® water each for 10 minutes at room temperature, followed by pure Milli-Q® water for 10 minutes at room temperature.

For H&E staining, sections were first incubated in filtered hematoxylin Harris (2E-056, Waldeck) for 5 minutes at room temperature, followed by rinsing in Milli-Q® water. Sections were differentiated in 0.185% HCl (124630010, Acros Organics) in Milli-Q® water by 4 quick immersions at room temperature, followed by rinsing in tap water. Bluing was performed in 0.015% ammonia water (1.05432.1000, Merck Millipore) by 6 quick immersions at room temperature, followed by rinsing in Milli-Q® water and 4 quick immersions in 70% ethanol at room temperature. Sections were incubated in 0.075% eosin (1B-425, Waldeck) + 0.0075% phloxin (15926.0025, Merck Millipore) + 0.5% acetic acid (1.00063.1011, Merck Millipore) + 84% ethanol in Milli-Q® water for 3 minutes at room temperature. After rinsing in 100% ethanol and xylene, they were finally covered with coverslips (01012227, Biosystems).

For antibody staining, a Ventana Bench Mark Ultra Plus fully automated staining machine (Roche) was used, containing the Bench Mark Ultra LCS staining kit. Staining was visualized with HRP DAB included in the kit. Slides were scanned using a Hamamatsu C9600 digital slide scanner (Hamamatsu Photonics).

### *3D light-sheet imaging*

Light-sheet imaging was performed using a custom-built mesoSPIM V5[29]. For all image settings, the following lasers and filter combinations were applied: 488 nm laser with a 520/35 BrightLine HC filter (AHF analysentechnik AG, part number #F37-520SG) or QuadLine Rejectionband ZET405/488/561/640 filter (AHF analysentechnik AG, part number

#F57-405SG); 561 nm laser with 561 Razor Edge LP filter (AHF analysentechnik AG, part number #F76-561) or QuadLine Rejectionband ZET405/488/561/640 filter; 640 nm laser with 647 Razor Edge LP Filter (AHF analysentechnik AG, part number #F76-647); 647 nm laser with QuadLine Rejectionband ZET405/488/561/640 filter. Laser intensities were individually set for the samples/each experiment to achieve the best SNR. For instance, for the autofluorescence removal experiment the same settings were used for all samples. For overview whole-mount 3D images, the 1x objective was used at zoom levels of 0.63x (pixel size: 10 µm/pixel), 1x (pixel size: 6 µm/pixel) or 2x (pixel size: 3 µm/pixel), depending on sample size. Camera exposure time was 10 ms. For high-magnification ROI imaging, a 2x objective (MVPLAPO2XC, Olympus/Evident) was used in combination with a dipping cap (205915, LaVision BioTec). The front cover glass of the dipping cap was removed and replaced with a 40×40×40 mm cuvette (Portmann Instruments). This objective was used at zoom levels of 2x (pixel size: 1.5 µm/pixel), 4x (pixel size: 0.75 µm/pixel) or 6.3x (pixel size: 0.5 µm/pixel). Alternatively, a modified detection path based on the Benchtop mesoSPIM (mesoSPIM V6) with a Mitutoyo objective turret (Mitutoyo) and a Mitutoyo G Plan Apo 20x objective (pixel size: 0.275 µm/pixel) was used[30]. Camera exposure time was 20 ms. Samples were imaged in a 40-mm cuvette filled with DBE ($n_D$ = 1.56) and z-step size was chosen to reach (near) isotropic voxel size.

For the use-case study, tile scanning of each entire cortex sample was performed with the 1x objective at 4x zoom (pixel size: 1.5 µm/pixel). Samples were imaged in a 30-mm cuvette filled with DBE. Camera exposure time was 10 ms.

### *Qualitative image processing*

For 3D data analysis, an AMD Ryzen W137 Threadripper PRO Workstation with 2x NVIDIA Geforce RTX 3090 24GB GDDR6X graphic cards (Brentford) was used. Fiji software (64 bit version 2.3.0/1.53f51[62]) was employed for main qualitative image processing, containing cropping, contrast adjustment, background subtraction, contrast limited adaptive histogram equalization (CLAHE), color and look up table (LUT) intensity assignment, channel merging, generation of hyperstacks with temporal color code, generation of substacks and maximum intensity projections, generation of videos, and scale bar assignments. The volume viewer plugin[63] was applied for volume rendering. The 3DScript plugin[64] was used for volume rendering and for generating complex video sequences via encoded video scripts. Adobe Premiere Elements (Adobe version 2021) was applied for further image and video processing, consisting of sharpening, brightening, video clipping and text labeling.

### *Mean fluorescence intensity (MFI) projection and z-profile*

Codes for the assessment of MFI projection and z-profile were written in MATLAB (MathWorks, version 2022b). For both calculations, the background of the sample was excluded by setting all background pixels without sample to not-a-number (NaN). The MFI projection was calculated as the mean projection value along the z-axis and plotted as heatmap in xy-direction. The z-profile was calculated as the mean fluorescence intensity for each imaging plane (in z) across the sample, with the standard error of the mean (s.e.m.) computed across the pixels of each plane.

### *Stitching*

3D image tiles were automatically stitched via a custom-written code in R studio (version 1.2.1335, R version 3.6.0[65]), using Fiji and TeraStitcher (version 1.11.6., ref. [66]).

### *Neuronal cell segmentation and detection*

To automatically and reliably detect neurons in human brain cortex, a three-step procedure was implemented in Python (versions 2.7. and 3.10.12, ref.[67, 68]). First, stitched raw stacks were segmented using a supervised random forest machine learning classifier (ILASTIK version 1.4.0rc6, ref.[40]) into coherent 3D particles that were then identified as initial neuronal cell candidates using an established cell detection pipeline (ClearMap 1.0, ref.[41]). To train the ILASTIK classifier, ground truth was manually annotated volumetrically as foreground vs. background in 13 representative substacks of 200 x 200 x 200 voxels. Representative substacks were generated from the entire 15 TB-sized data set, representing various regions (transitions of different cortical layers and white matter, regions with high and lower SNR) from different samples (controls and FCD patients). To fit the input into the memory for ILASTIK processing, the ClearMap pipeline was parallelized. Segmentation was performed such that overdetection was more likely than underdetection to enable subsequent refinement by discarding false positives. Refinement of cell candidates is conceptually similar to an existing pipeline[69] for murine cell detection, but has been implemented independently and adapted to our human data. Initial neuronal cell candidates were detected based on local intensity maxima using ClearMap. For quality checks, results were visualized in Fiji (64 bit version 2.3.0/1.53f51[62]). Second, initial cell candidates were merged using a custom-written 3D-peak finder based on 3D gradient ascent. Briefly, for each initial neuronal cell candidate determined by ClearMap in step 1, the local raw 3D image (31 x 31 x 91 voxels in xyz) was extracted and smoothed with a Gaussian filter (standard deviation of 1.0, 1.0, and 2.5 pixels in x-, y-, and z-direction, respectively). Within this local environment, the position of the detected cell was iteratively optimized to follow the maximum image intensity until the algorithm converged to a local maximum. Upon this gradient-based refinement of neuron

positions, cells that ended up at the same maximum were merged. Code for gradient-based refinement and merging of neuronal cell candidates is available on Github: https://github.com/PTRRupprecht/Cell_Detection/tree/main/Gradient_cell_merger. Third, the refined neuronal cell candidates were classified as cells or non-cells using a DCNN-based binary classifier. This procedure served to exclude non-neuronal somata bright structures such as proximal axons, hot pixels of the camera sensor, or spurious noise. Briefly, each 100 neuronal cell candidates as output from the second processing step were chosen at random from 19 different 3D samples, resulting in a total of 1900 neuronal cell candidates for ground truth annotation and validation. These neuronal cell candidates were manually annotated by visually inspecting xy-sections (31 x 31 pixels) and xz-sections (31 x 91 pixels), centered at the location of the candidate cell. Each neuronal cell candidate was assigned either a “cell” or “non-cell” label. A Python-based interactive tool used to perform these annotations is available on Github: https://github.com/PTRRupprecht/Cell_Detection/tree/main/Label_tool. Next, DCNNs were trained based on the annotated ground truth to predict whether a detected neuronal cell candidate was a cell. Three networks for different sections (xy, xz, yz) were combined by adding their outputs. All networks were standard convolutional networks with two 2D convolutional layers with ReLu activation units, followed each by a 2 x 2 max pooling layer, a subsequent set of two dense layers with ReLu activation units, and a final layer with 2 neurons. These two output neurons represented the two classes (“cell” and “non-cell”). The network was defined in PyTorch[70] and trained with a standard Adagrad[71] optimizer, using cross entropy loss with a batch size of 10. The classification performance plateaued after approximately 1500 training epochs (Extended Data Fig. 5c). 1800 randomly selected neuronal cell candidates were used for training. Performance was evaluated using cross-validation with randomly selected withheld neuronal cell candidates (100 random cell candidates withheld of a total of 1900). To improve cell classification, averaging across deep network ensembles was used[72]. Five instantiations of each network type (xy, xz, yz) were trained and their predictions were linearly combined for ensemble averaging across 15 models. Based on ensemble predictions, neuronal cell candidates were accepted or discarded. In cross-validated performance evaluation, the classifier was correct for 92.2% of neuronal cell candidates and incorrect for 7.8%, with false positives and false negatives at 4.2% and 3.6%, respectively. Python code to train and apply the neuronal cell candidate classifier together with an example ground truth data set of manually annotated neuronal cell candidates is available on Github:
https://github.com/PTRRupprecht/Cell_Detection/tree/main/Binary_classification_neuron_candidates.

### *Quantification of neuronal density*

To quantify neuronal density, neurons in the 3D stack were detected as described above, yielding the total number of detected neurons. Subsequently, the number of detected neurons was divided by the volume occupied by the brain sample. The volume of the brain sample was obtained by a binary 3D mask computed in Python, using a manually defined global threshold. The resulting 3D mask was corrected and refined by manual annotation of the 12x-downsampled segmented stack in 3D with three interactive views (xy, xz, yz) using ITK-SNAP (version 3.6.0, ref.[73]). To distinguish cortical vs. white matter brain volumes, cortical regions of 12x-downsampled imaging stacks were manually annotated in 3D with three interactive views (xy, xz, yz) using ITK-SNAP (version 3.6.0). Manual annotation of focal neuronal loss regions was performed in ITK-SNAP (version 4.0.1) by carefully inspecting the 4x-downsampled brain tissue blocks in 3D with three interactive views (xy, xz, yz).

### *Neuronal cell density profiles across cortical layers*

To assign “cortical depth” normalized to each position in a stack by the local cortical thickness, landmarks within the cortical sample were annotated, hyperplane fits of these annotations applied, and the distance between these hyperplanes scaled to normalize for cortical thickness. First, to annotate landmarks, we identified the outer brain boundary, the boundary between cortical layers 1 and 2, the stripe of increased neuronal density in layer 4, and the boundary between layer 6 and the white matter. Xy-sections were manually annotated with 5-8 coordinates for the respective landmark in a custom-written interactive Python script. Every 100 pixels (100 µm) in the z-direction, an xy-section was annotated, and a 3$^{rd}$ order polynomial hyperplane was fitted to each of the landmark layers. For each neuron in the 3D volume, the shortest distance to each of the landmark hyperplanes was determined, which enabled the computation of the local relative distance between two landmark layers.

### *Figure design*

Figures were designed in Affinity Designer 2 (version 2.3.1). CAD models were designed in Autodesk Inventor (version 2023).

## References


(1) Sukswai, N.; Khoury, J. D. Immunohistochemistry Innovations for Diagnosis and Tissue-Based Biomarker Detection. *Curr Hematol Malig Rep* **2019**, *14* (5), 368-375. DOI: 10.1007/s11899-019-00533-9.

(2) Ittmann, M. Anatomy and Histology of the Human and Murine Prostate. *Cold Spring Harb Perspect Med* **2018**, *8* (5). DOI: 10.1101/cshperspect.a030346.

(3) Blum, F. Über Formaldehyd als Härtungsmittel. *Zentralblatt für allgemeine Pathologie und pathologische Anatomie* **1893**, *4*, 1-14.

(4) Sy, J.; Ang, L. C. Microtomy: Cutting Formalin-Fixed, Paraffin-Embedded Sections. *Methods Mol Biol* **2019**, *1897*, 269-278. DOI: 10.1007/978-1-4939-8935-5_23.

(5) Tainaka, K.; Kuno, A.; Kubota, S. I.; Murakami, T.; Ueda, H. R. Chemical Principles in Tissue Clearing and Staining Protocols for Whole-Body Cell Profiling. *Annu Rev Cell Dev Biol* **2016**, *32*, 713-741. DOI: 10.1146/annurev-cellbio-111315-125001.

(6) Ueda, H. R.; Ertürk, A.; Chung, K.; Gradinaru, V.; Chédotal, A.; Tomancak, P.; Keller, P. J. Tissue clearing and its applications in neuroscience. *Nat Rev Neurosci* **2020**, *21* (2), 61-79. DOI: 10.1038/s41583-019-0250-1.

(7) DAVISON, A. N.; WAJDA, M. Analysis of lipids from fresh and preserved adult human brains. *Biochem J* **1962**, *82* (1), 113-117. DOI: 10.1042/bj0820113.

(8) Inoue, M.; Saito, R.; Kakita, A.; Tainaka, K. Rapid chemical clearing of white matter in the post-mortem human brain by 1,2-hexanediol delipidation. *Bioorg Med Chem Lett* **2019**, *29* (15), 1886-1890. DOI: 10.1016/j.bmcl.2019.05.049.

(9) Molina, L. M.; Krutsenko, Y.; Jenkins, N. E. C.; Smith, M. C.; Tao, J.; Wheeler, T. B.; Watkins, S. C.; Watson, A. M.; Monga, S. P. LiverClear: A versatile protocol for mouse liver tissue clearing. *STAR Protoc* **2022**, *3* (1), 101178. DOI: 10.1016/j.xpro.2022.101178.

(10) Renier, N.; Wu, Z.; Simon, D. J.; Yang, J.; Ariel, P.; Tessier-Lavigne, M. iDISCO: a simple, rapid method to immunolabel large tissue samples for volume imaging. *Cell* **2014**, *159* (4), 896-910. DOI: 10.1016/j.cell.2014.10.010.

(11) Belle, M.; Godefroy, D.; Couly, G.; Malone, S. A.; Collier, F.; Giacobini, P.; Chédotal, A. Tridimensional Visualization and Analysis of Early Human Development. *Cell* **2017**, *169* (1), 161-173.e112. DOI: 10.1016/j.cell.2017.03.008.

(12) Scalia, C. R.; Boi, G.; Bolognesi, M. M.; Riva, L.; Manzoni, M.; DeSmedt, L.; Bosisio, F. M.; Ronchi, S.; Leone, B. E.; Cattoretti, G. Antigen Masking During Fixation and Embedding, Dissected. *J Histochem Cytochem* **2017**, *65* (1), 5-20. DOI: 10.1369/0022155416673995.

(13) Liebmann, T.; Renier, N.; Bettayeb, K.; Greengard, P.; Tessier-Lavigne, M.; Flajolet, M. Three-Dimensional Study of Alzheimer's Disease Hallmarks Using the iDISCO Clearing Method. *Cell Rep* **2016**, *16* (4), 1138-1152. DOI: 10.1016/j.celrep.2016.06.060.

(14) Tanaka, N.; Kanatani, S.; Tomer, R.; Sahlgren, C.; Kronqvist, P.; Kaczynska, D.; Louhivuori, L.; Kis, L.; Lindh, C.; Mitura, P.; et al. Whole-tissue biopsy phenotyping of three-dimensional tumours reveals patterns of cancer heterogeneity. *Nat Biomed Eng* **2017**, *1* (10), 796-806. DOI: 10.1038/s41551-017-0139-0.

(15) Hildebrand, S.; Schueth, A.; Herrler, A.; Galuske, R.; Roebroeck, A. Scalable Labeling for Cytoarchitectonic Characterization of Large Optically Cleared Human Neocortex Samples. *Sci Rep* **2019**, *9* (1), 10880. DOI: 10.1038/s41598-019-47336-9.

(16) Schueth, A.; Hildebrand, S.; Samarska, I.; Sengupta, S.; Kiessling, A.; Herrler, A.; Zur Hausen, A.; Capalbo, M.; Roebroeck, A. Efficient 3D light-sheet imaging of very large-scale optically cleared human brain and prostate tissue samples. *Commun Biol* **2023**, *6* (1), 170. DOI: 10.1038/s42003-023-04536-4.

(17) Zhao, S.; Todorov, M. I.; Cai, R.; -Maskari, R. A.; Steinke, H.; Kemter, E.; Mai, H.; Rong, Z.; Warmer, M.; Stanic, K.; et al. Cellular and Molecular Probing of Intact Human Organs. *Cell* **2020**, *180* (4), 796-812.e719. DOI: 10.1016/j.cell.2020.01.030.

(18) Mai, H.; Rong, Z.; Zhao, S.; Cai, R.; Steinke, H.; Bechmann, I.; Ertürk, A. Scalable tissue labeling and clearing of intact human organs. *Nat Protoc* **2022**, *17* (10), 2188-2215. DOI: 10.1038/s41596-022-00712-8.

(19) Lai, H. M.; Liu, A. K. L.; Ng, H. H. M.; Goldfinger, M. H.; Chau, T. W.; DeFelice, J.; Tilley, B. S.; Wong, W. M.; Wu, W.; Gentleman, S. M. Next generation histology methods for three-

dimensional imaging of fresh and archival human brain tissues. *Nat Commun* **2018**, *9* (1), 1066. DOI: 10.1038/s41467-018-03359-w.
(20) Liu, A. K. L.; Lai, H. M.; Chang, R. C.; Gentleman, S. M. Free of acrylamide sodium dodecyl sulphate (SDS)-based tissue clearing (FASTClear): a novel protocol of tissue clearing for three-dimensional visualization of human brain tissues. *Neuropathol Appl Neurobiol* **2017**, *43* (4), 346-351. DOI: 10.1111/nan.12361.
(21) Perbellini, F.; Liu, A. K. L.; Watson, S. A.; Bardi, I.; Rothery, S. M.; Terracciano, C. M. Free-of-Acrylamide SDS-based Tissue Clearing (FASTClear) for three dimensional visualization of myocardial tissue. *Sci Rep* **2017**, *7* (1), 5188. DOI: 10.1038/s41598-017-05406-w.
(22) Chung, K.; Wallace, J.; Kim, S. Y.; Kalyanasundaram, S.; Andalman, A. S.; Davidson, T. J.; Mirzabekov, J. J.; Zalocusky, K. A.; Mattis, J.; Denisin, A. K.; et al. Structural and molecular interrogation of intact biological systems. *Nature* **2013**, *497* (7449), 332-337. DOI: 10.1038/nature12107.
(23) Morawski, M.; Kirilina, E.; Scherf, N.; Jäger, C.; Reimann, K.; Trampel, R.; Gavriilidis, F.; Geyer, S.; Biedermann, B.; Arendt, T.; et al. Developing 3D microscopy with CLARITY on human brain tissue: Towards a tool for informing and validating MRI-based histology. *Neuroimage* **2018**, *182*, 417-428. DOI: 10.1016/j.neuroimage.2017.11.060.
(24) Murray, E.; Cho, J. H.; Goodwin, D.; Ku, T.; Swaney, J.; Kim, S. Y.; Choi, H.; Park, Y. G.; Park, J. Y.; Hubbert, A.; et al. Simple, Scalable Proteomic Imaging for High-Dimensional Profiling of Intact Systems. *Cell* **2015**, *163* (6), 1500-1514. DOI: 10.1016/j.cell.2015.11.025.
(25) Park, Y. G.; Sohn, C. H.; Chen, R.; McCue, M.; Yun, D. H.; Drummond, G. T.; Ku, T.; Evans, N. B.; Oak, H. C.; Trieu, W.; et al. Protection of tissue physicochemical properties using polyfunctional crosslinkers. *Nat Biotechnol* **2018**. DOI: 10.1038/nbt.4281.
(26) Lin, Y. H.; Wang, L. W.; Chen, Y. H.; Chan, Y. C.; Hu, S. H.; Wu, S. Y.; Chiang, C. S.; Huang, G. J.; Yang, S. D.; Chu, S. W.; et al. Revealing intact neuronal circuitry in centimeter-sized formalin-fixed paraffin-embedded brain. *Elife* **2024**, *13*. DOI: 10.7554/eLife.93212.
(27) Ku, T.; Guan, W.; Evans, N. B.; Sohn, C. H.; Albanese, A.; Kim, J. G.; Frosch, M. P.; Chung, K. Elasticizing tissues for reversible shape transformation and accelerated molecular labeling. *Nat Methods* **2020**, *17* (6), 609-613. DOI: 10.1038/s41592-020-0823-y.
(28) Nojima, S.; Susaki, E. A.; Yoshida, K.; Takemoto, H.; Tsujimura, N.; Iijima, S.; Takachi, K.; Nakahara, Y.; Tahara, S.; Ohshima, K.; et al. CUBIC pathology: three-dimensional imaging for pathological diagnosis. *Sci Rep* **2017**, *7* (1), 9269. DOI: 10.1038/s41598-017-09117-0.
(29) Voigt, F. F.; Kirschenbaum, D.; Platonova, E.; Pages, S.; Campbell, R. A. A.; Kastli, R.; Schaettin, M.; Egolf, L.; van der Bourg, A.; Bethge, P.; et al. The mesoSPIM initiative: open-source light-sheet microscopes for imaging cleared tissue. *Nat Methods* **2019**, *16* (11), 1105-1108. DOI: 10.1038/s41592-019-0554-0.
(30) Vladimirov, N.; Voigt, F. F.; Naert, T.; Araujo, G. R.; Cai, R.; Reuss, A. M.; Zhao, S.; Schmid, P.; Hildebrand, S.; Schaettin, M.; et al. Benchtop mesoSPIM: a next-generation open-source light-sheet microscope for cleared samples. *Nat Commun* **2024**, *15* (1), 2679. DOI: 10.1038/s41467-024-46770-2 From NLM Medline.
(31) Tan, Y.; Chiam, C. P. L.; Zhang, Y.; Tey, H. L.; Ng, L. G. Research Techniques Made Simple: Optical Clearing and Three-Dimensional Volumetric Imaging of Skin Biopsies. *J Invest Dermatol* **2020**, *140* (7), 1305-1314.e1301. DOI: 10.1016/j.jid.2020.04.014.
(32) Schnell, S. A.; Staines, W. A.; Wessendorf, M. W. Reduction of lipofuscin-like autofluorescence in fluorescently labeled tissue. *J Histochem Cytochem* **1999**, *47* (6), 719-730. DOI: 10.1177/002215549904700601.
(33) Susaki, E. A.; Tainaka, K.; Perrin, D.; Yukinaga, H.; Kuno, A.; Ueda, H. R. Advanced CUBIC protocols for whole-brain and whole-body clearing and imaging. *Nat Protoc* **2015**, *10* (11), 1709-1727. DOI: 10.1038/nprot.2015.085.
(34) Hama, H.; Hioki, H.; Namiki, K.; Hoshida, T.; Kurokawa, H.; Ishidate, F.; Kaneko, T.; Akagi, T.; Saito, T.; Saido, T.; et al. ScaleS: an optical clearing palette for biological imaging. *Nat Neurosci* **2015**, *18* (10), 1518-1529. DOI: 10.1038/nn.4107.
(35) Cai, R.; Pan, C.; Ghasemigharagoz, A.; Todorov, M. I.; Förstera, B.; Zhao, S.; Bhatia, H. S.; Parra-Damas, A.; Mrowka, L.; Theodorou, D.; et al. Panoptic imaging of transparent mice

reveals whole-body neuronal projections and skull-meninges connections. *Nat Neurosci* **2019**, *22* (2), 317-327. DOI: 10.1038/s41593-018-0301-3.
(36) Molnár, Z.; Clowry, G. J.; Šestan, N.; Alzu'bi, A.; Bakken, T.; Hevner, R. F.; Hüppi, P. S.; Kostović, I.; Rakic, P.; Anton, E. S.; et al. New insights into the development of the human cerebral cortex. *J Anat* **2019**, *235* (3), 432-451. DOI: 10.1111/joa.13055.
(37) Cajal, S. R. y. *Comparative*
*study of the sensory areas of the human cortex*; Clark University, 1899.
(38) Leuba, G.; Garey, L. J. Evolution of neuronal numerical density in the developing and aging human visual cortex. *Hum Neurobiol* **1987**, *6* (1), 11-18.
(39) Gittins, R.; Harrison, P. J. Neuronal density, size and shape in the human anterior cingulate cortex: a comparison of Nissl and NeuN staining. *Brain Res Bull* **2004**, *63* (2), 155-160. DOI: 10.1016/j.brainresbull.2004.02.005.
(40) Berg, S.; Kutra, D.; Kroeger, T.; Straehle, C. N.; Kausler, B. X.; Haubold, C.; Schiegg, M.; Ales, J.; Beier, T.; Rudy, M.; et al. ilastik: interactive machine learning for (bio)image analysis. *Nat Methods* **2019**, *16* (12), 1226-1232. DOI: 10.1038/s41592-019-0582-9.
(41) Renier, N.; Adams, E. L.; Kirst, C.; Wu, Z.; Azevedo, R.; Kohl, J.; Autry, A. E.; Kadiri, L.; Umadevi Venkataraju, K.; Zhou, Y.; et al. Mapping of Brain Activity by Automated Volume Analysis of Immediate Early Genes. *Cell* **2016**, *165* (7), 1789-1802. DOI: 10.1016/j.cell.2016.05.007.
(42) Kabat, J.; Król, P. Focal cortical dysplasia - review. *Pol J Radiol* **2012**, *77* (2), 35-43. DOI: 10.12659/pjr.882968.
(43) ILAE Commission Report. The epidemiology of the epilepsies: future directions. International League Against Epilepsy. *Epilepsia* **1997**, *38* (5), 614-618.
(44) Bast, T.; Ramantani, G.; Seitz, A.; Rating, D. Focal cortical dysplasia: prevalence, clinical presentation and epilepsy in children and adults. *Acta Neurol Scand* **2006**, *113* (2), 72-81. DOI: 10.1111/j.1600-0404.2005.00555.x.
(45) Blümcke, I.; Thom, M.; Aronica, E.; Armstrong, D. D.; Vinters, H. V.; Palmini, A.; Jacques, T. S.; Avanzini, G.; Barkovich, A. J.; Battaglia, G.; et al. The clinicopathologic spectrum of focal cortical dysplasias: a consensus classification proposed by an ad hoc Task Force of the ILAE Diagnostic Methods Commission. *Epilepsia* **2011**, *52* (1), 158-174. DOI: 10.1111/j.1528-1167.2010.02777.x.
(46) Blumcke, I.; Budday, S.; Poduri, A.; Lal, D.; Kobow, K.; Baulac, S. Neocortical development and epilepsy: insights from focal cortical dysplasia and brain tumours. *Lancet Neurol* **2021**, *20* (11), 943-955. DOI: 10.1016/S1474-4422(21)00265-9.
(47) Chong, S.; Phi, J. H.; Lee, J. Y.; Kim, S. K. Surgical Treatment of Lesional Mesial Temporal Lobe Epilepsy. *J Epilepsy Res* **2018**, *8* (1), 6-11. DOI: 10.14581/jer.18002.
(48) Widdess-Walsh, P.; Diehl, B.; Najm, I. Neuroimaging of focal cortical dysplasia. *J Neuroimaging* **2006**, *16* (3), 185-196. DOI: 10.1111/j.1552-6569.2006.00025.x.
(49) Heers, M.; Helias, M.; Hedrich, T.; Dümpelmann, M.; Schulze-Bonhage, A.; Ball, T. Spectral bandwidth of interictal fast epileptic activity characterizes the seizure onset zone. *Neuroimage Clin* **2018**, *17*, 865-872. DOI: 10.1016/j.nicl.2017.11.021.
(50) Glaser, A. K.; Bishop, K. W.; Barner, L. A.; Susaki, E. A.; Kubota, S. I.; Gao, G.; Serafin, R. B.; Balaram, P.; Turschak, E.; Nicovich, P. R.; et al. A hybrid open-top light-sheet microscope for versatile multi-scale imaging of cleared tissues. *Nat Methods* **2022**, *19* (5), 613-619. DOI: 10.1038/s41592-022-01468-5.
(51) Tan, Y.; Ng, W. J.; Lee, S. Z. X.; Lee, B. T. K.; Nattkemper, L. A.; Yosipovitch, G.; Ng, L. G.; Tey, H. L. 3-Dimensional Optical Clearing and Imaging of Pruritic Atopic Dermatitis and Psoriasis Skin Reveals Downregulation of Epidermal Innervation. *J Invest Dermatol* **2019**, *139* (5), 1201-1204. DOI: 10.1016/j.jid.2018.11.006.
(52) Abadie, S.; Jardet, C.; Colombelli, J.; Chaput, B.; David, A.; Grolleau, J. L.; Bedos, P.; Lobjois, V.; Descargues, P.; Rouquette, J. 3D imaging of cleared human skin biopsies using light-sheet microscopy: A new way to visualize in-depth skin structure. *Skin Res Technol* **2018**, *24* (2), 294-303. DOI: 10.1111/srt.12429.
(53) Jeong, J.; Tanaka, M.; Yang, Y.; Arefyev, N.; DiRito, J.; Tietjen, G.; Zhang, X.; McConnell, M. J.; Utsumi, T.; Iwakiri, Y. An optimized visualization and quantitative protocol for in-depth evaluation of lymphatic vessel architecture in the liver. *Am J Physiol Gastrointest Liver Physiol* **2023**, *325* (5), G379-G390. DOI: 10.1152/ajpgi.00139.2023.

(54) Chen, C. C.; Peng, S. J.; Chou, Y. H.; Lee, C. Y.; Lee, P. H.; Hu, R. H.; Ho, M. C.; Chung, M. H.; Hsiao, F. T.; Tien, Y. W.; et al. Human liver afferent and efferent nerves revealed by 3-D/Airyscan super-resolution imaging. *Am J Physiol Endocrinol Metab* **2024**, *326* (2), E107-E123. DOI: 10.1152/ajpendo.00205.2023.
(55) Yoshizawa, T.; Lee, J. W.; Hong, S. M.; Jung, D.; Noë, M.; Zbijewski, W.; Kiemen, A.; Wu, P. H.; Wirtz, D.; Hruban, R. H.; et al. Three-dimensional analysis of ductular reactions and their correlation with liver regeneration and fibrosis. *Virchows Arch* **2024**, *484* (5), 753-763. DOI: 10.1007/s00428-023-03641-3.
(56) Fabyan, W. B.; Fortin, C. L.; Kenerson, H. L.; Simmonds, S. P.; Liu, J. T. C.; Yeh, M. M.; Carr, R. M.; Yeung, R. S. W.; Stevens, K. R. LiverMap pipeline for 3D imaging of human liver reveals volumetric spatial dysregulation of cirrhotic vasculobiliary architecture. *bioRxiv* **2024**. DOI: 10.1101/2024.09.14.613049.
(57) Adori, C.; Daraio, T.; Kuiper, R.; Barde, S.; Horvathova, L.; Yoshitake, T.; Ihnatko, R.; Valladolid-Acebes, I.; Vercruysse, P.; Wellendorf, A. M.; et al. Disorganization and degeneration of liver sympathetic innervations in nonalcoholic fatty liver disease revealed by 3D imaging. *Sci Adv* **2021**, *7* (30). DOI: 10.1126/sciadv.abg5733.
(58) Kong, C.; Bobe, S.; Pilger, C.; Lachetta, M.; Øie, C. I.; Kirschnick, N.; Mönkemöller, V.; Hübner, W.; Förster, C.; Schüttpelz, M.; et al. Multiscale and Multimodal Optical Imaging of the Ultrastructure of Human Liver Biopsies. *Front Physiol* **2021**, *12*, 637136. DOI: 10.3389/fphys.2021.637136.
(59) Weiss, K. R.; Voigt, F. F.; Shepherd, D. P.; Huisken, J. Tutorial: practical considerations for tissue clearing and imaging. *Nat Protoc* **2021**, *16* (6), 2732-2748. DOI: 10.1038/s41596-021-00502-8.
(60) Thom, M.; Martinian, L.; Sen, A.; Cross, J. H.; Harding, B. N.; Sisodiya, S. M. Cortical neuronal densities and lamination in focal cortical dysplasia. *Acta Neuropathol* **2005**, *110* (4), 383-392. DOI: 10.1007/s00401-005-1062-0.
(61) Galvão, I. C.; Kandratavicius, L.; Messias, L. A.; Athié, M. C. P.; Assis-Mendonça, G. R.; Alvim, M. K. M.; Ghizoni, E.; Tedeschi, H.; Yasuda, C. L.; Cendes, F.; et al. Identifying cellular markers of focal cortical dysplasia type II with cell-type deconvolution and single-cell signatures. *Sci Rep* **2023**, *13* (1), 13321. DOI: 10.1038/s41598-023-40240-3.
(62) Schindelin, J.; Arganda-Carreras, I.; Frise, E.; Kaynig, V.; Longair, M.; Pietzsch, T.; Preibisch, S.; Rueden, C.; Saalfeld, S.; Schmid, B.; et al. Fiji: an open-source platform for biological-image analysis. *Nat Methods* **2012**, *9* (7), 676-682. DOI: 10.1038/nmeth.2019.
(63) Schmid, B.; Schindelin, J.; Cardona, A.; Longair, M.; Heisenberg, M. A high-level 3D visualization API for Java and ImageJ. *BMC Bioinformatics* **2010**, *11*, 274. DOI: 10.1186/1471-2105-11-274.
(64) Schmid, B.; Tripal, P.; Winter, Z.; Palmisano, R. 3Dscript.server: true server-side 3D animation of microscopy images using a natural language-based syntax. *Bioinformatics* **2021**, *37* (24), 4901-4902. DOI: 10.1093/bioinformatics/btab462.
(65) Team, R. C. R: A language and environment for statistical computing. R Foundation for Statistical Computing, Vienna, Austria.: 2020.
(66) Bria, A.; Iannello, G. TeraStitcher - a tool for fast automatic 3D-stitching of teravoxel-sized microscopy images. *BMC Bioinformatics* **2012**, *13*, 316. DOI: 10.1186/1471-2105-13-316.
(67) Van Rossum, G., & Drake Jr, F. L. *Python reference manual*. Centrum voor Wiskunde en Informatica Amsterdam: 1995.
(68) Van Rossum, G., & Drake, F. L. *Python 3 Reference Manual*. Scotts Valley, CA: CreateSpace: 2009.
(69) Tyson, A. L.; Rousseau, C. V.; Niedworok, C. J.; Keshavarzi, S.; Tsitoura, C.; Cossell, L.; Strom, M.; Margrie, T. W. A deep learning algorithm for 3D cell detection in whole mouse brain image datasets. *PLoS Comput Biol* **2021**, *17* (5), e1009074. DOI: 10.1371/journal.pcbi.1009074.
(70) Paszke, A. e. a. PyTorch: An Imperative Style, High-Performance Deep Learning Library. Advances in Neural Information Processing Systems: 2019; Vol. 32, pp 8024-8035.
(71) Duchi, J., Hazan, E., & Singer, Y. Adaptive subgradient methods for online learning and stochastic optimization. Journal of machine learning research: 2011; Vol. 12.

(72) Fort, S., Huiyi Hu, and Balaji Lakshminarayanan. Deep ensembles: A loss landscape perspective. arXiv preprint: 2019; Vol. arXiv:1912.02757.
(73) Yushkevich, P. A.; Piven, J.; Hazlett, H. C.; Smith, R. G.; Ho, S.; Gee, J. C.; Gerig, G. User-guided 3D active contour segmentation of anatomical structures: significantly improved efficiency and reliability. *Neuroimage* **2006**, *31* (3), 1116-1128. DOI: 10.1016/j.neuroimage.2006.01.015.

## Acknowledgements

We thank Irina Abakumova and Mirella Woodert for technical help with conventional 2D histology. We express our gratitude to José Maria Mateos Melero from the Center for Microscopy and Image Analysis, Zurich (ZMB) for technical assistance in light-sheet microscopy, and to André Wethmar for support in IT infrastructure. Furthermore, Florence Gillieron, Karen Sadoyama, and Magdalena Kloyer are kindly acknowledged for assistance in 3D image annotations. We thank Susanne Dettwiler for help in FFPE human sample selection from the diagnostic archive. Finally, we highly appreciate Viktor Koelzer's expert input for figure design. This work was supported by the EMPIRIS and Lazarus grants, University Hospital Zurich Foundation, by the Investment Fund, University of Zurich, and by the Filling-the-Gap grant, University of Zurich (A.M.R. and A.A.). Furthermore, this work was supported by the University Research Priority Program (URPP) "Adaptive Brain Circuits in Development and Learning (AdaBD)" of the University of Zurich (N.V. and F.H.).

## Author contributions

A.M.R. designed the project, developed the protocol, conducted experiments, performed SPIM imaging, analyzed data, created movies, and wrote the manuscript with input from all co-authors. P.R. established the 3D data analysis pipeline, analyzed the data of the use-case study with help and input by A.M.R., and contributed extensively to the manuscript write-up. D.G. helped with data analysis, created movies, drew the cartoons, and contributed to the manuscript write-up. M.C. provided shared technical help in conducting experiments and SPIM imaging. L.N. provided shared technical help in conducting experiments. L.F. established the stitching code. F.F.V. and N.V. built the mesoSPIMs, designed the CAD figures, and provided continuous support together with P.B. R.R. wrote the ethical permit for this project with input by A.M.R. F.H. provided funding and expert input to the project. A.A. provided the original idea, supervised the project, applied for funding, and contributed extensively to the manuscript write-up.

## Disclosures and competing interest

The authors declare no competing interests.

## Extended Data

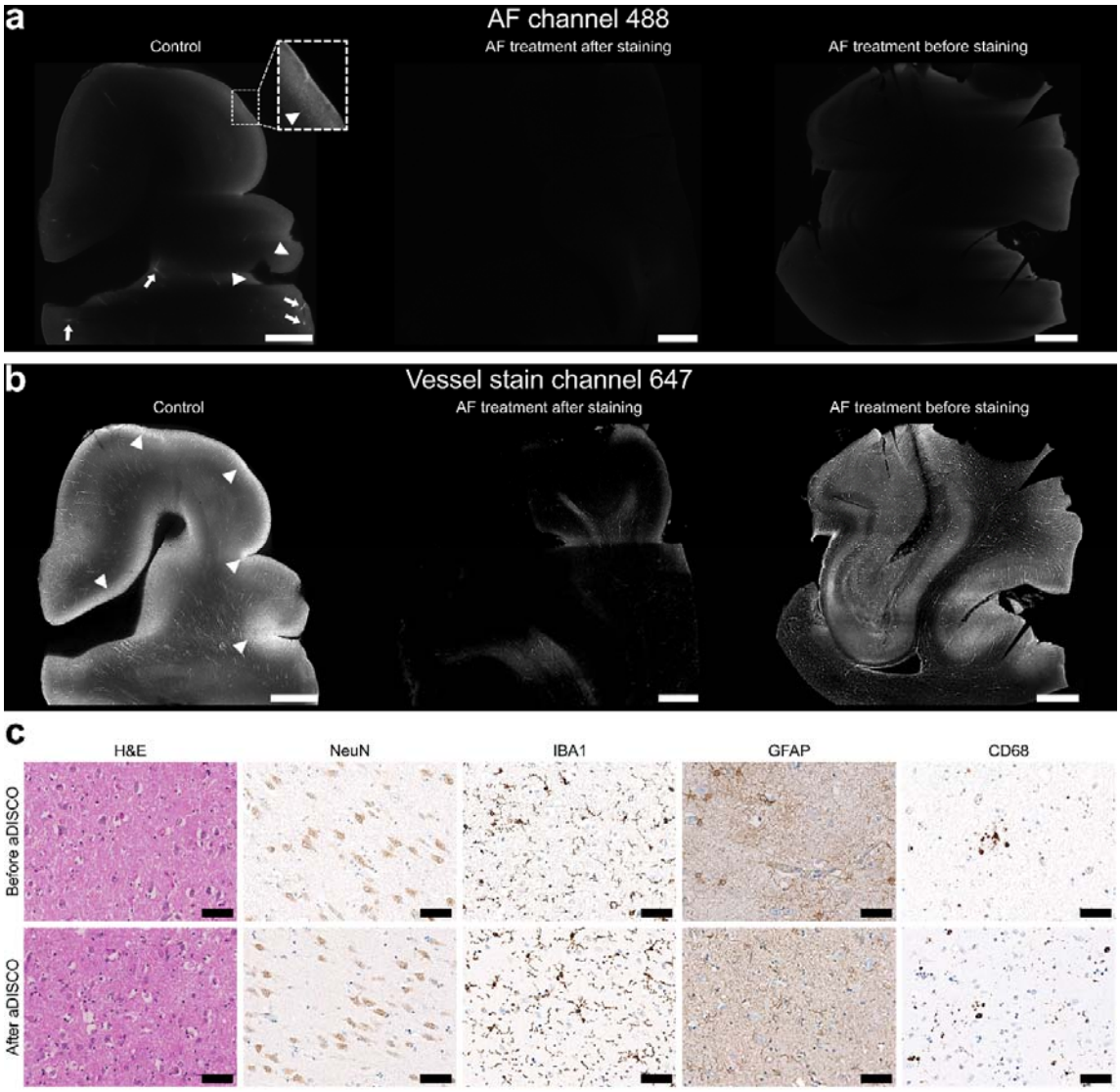


**Extended Data Figure 1. Details of aDISCO-processed archival human sample quality at distinct steps.**

**a**, Autofluorescence (AF) removal in archival human brain cortex sample imaged at 0.63x magnification using mesoSPIM V5. All samples were imaged and processed with the same settings. Unstained AF channel at 488 nm wavelength, displaying autofluorescent artifacts in the control sample, which arise from single vessels with coagulated blood (arrows) as well as from lipofuscin (arrowheads) despite bleaching with 28% hydrogen peroxide. Both AF treatment after and before staining remove autofluorescent artifacts. Scale bars: 2 mm. **b**, Preservation of stained signal by AF treatment in archival human brain cortex sample imaged at 0.63x magnification using mesoSPIM V5. All samples were imaged and processed with the same settings. Vessel channel at 647 nm wavelength, stained for the vasculature via CD13 antibody. In the control sample, lipofuscin autofluorescence in the cortex interferes with the stained vessel signal (arrowheads). While the stained vessel signal is substantially reduced by AF treatment after staining, it is preserved by AF treatment before staining. Scale bars: 2 mm. **c**, Conventional 2D histology before and after aDISCO processing. 2-µm thin sections cut from the same human brain cortex FFPE tissue block before and after aDISCO processing, stained for hematoxylin and eosin (H&E) as well as for different antibodies, and imaged using a Hamamatsu C9600 digital slide scanner. Scale bars: 50 µm.

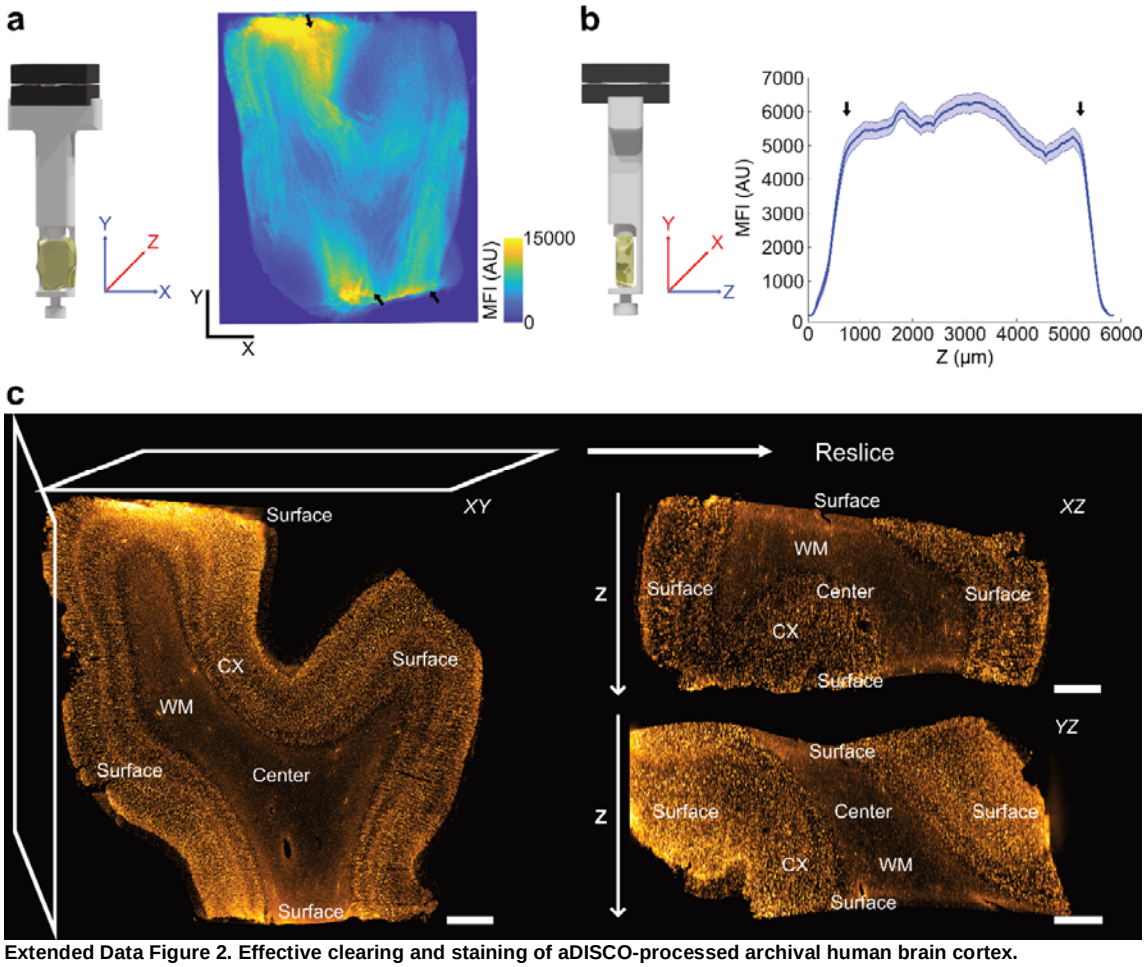


**Extended Data Figure 2. Effective clearing and staining of aDISCO-processed archival human brain cortex.**

**a**, Mean fluorescence intensity (MFI) projection averaged over all planes in z (red axis) and plotted as heatmap in xy (blue axes), as illustrated by the computer-aided design (CAD) model. Focal high-intensity pixels at top and bottom are due to screwing of the sample to the holder for imaging (black arrows). Color scale indicates MFI range in arbitrary units (AU). Scale bars: 2 mm. **b**, Z-profile of mean fluorescence intensity (MFI) in arbitrary units (AU), averaged over all xy-pixels (red axes) per imaging plane and plotted along the z-axis (blue) with s.e.m. (light blue), as illustrated by the computer-aided design (CAD) model. Arrows indicate beginning and end of sample. **c**, Archival human brain cortex sample, stained for neurons via anti-NeuN antibody, and imaged at 1.25x magnification using mesoSPIM V5 . Left: Slice in xy-projection from the sample center in z-direction. Right: Slice in xz- (top) and yz-projection (bottom) from the sample center in y- and x-direction, respectively, generated via reslicing of the 3D stack. In all three projections, continuous staining signal in the cortex (CX) from the surfaces to the center as well as effective (non-blurry) clearing of the neuron-poor white matter (WM) can be observed. This continuity through the sample thickness is particularly visible in the resliced xz- (top) and yz-projection (bottom) along the z-axis (z arrows). Scale bars: 1 mm.

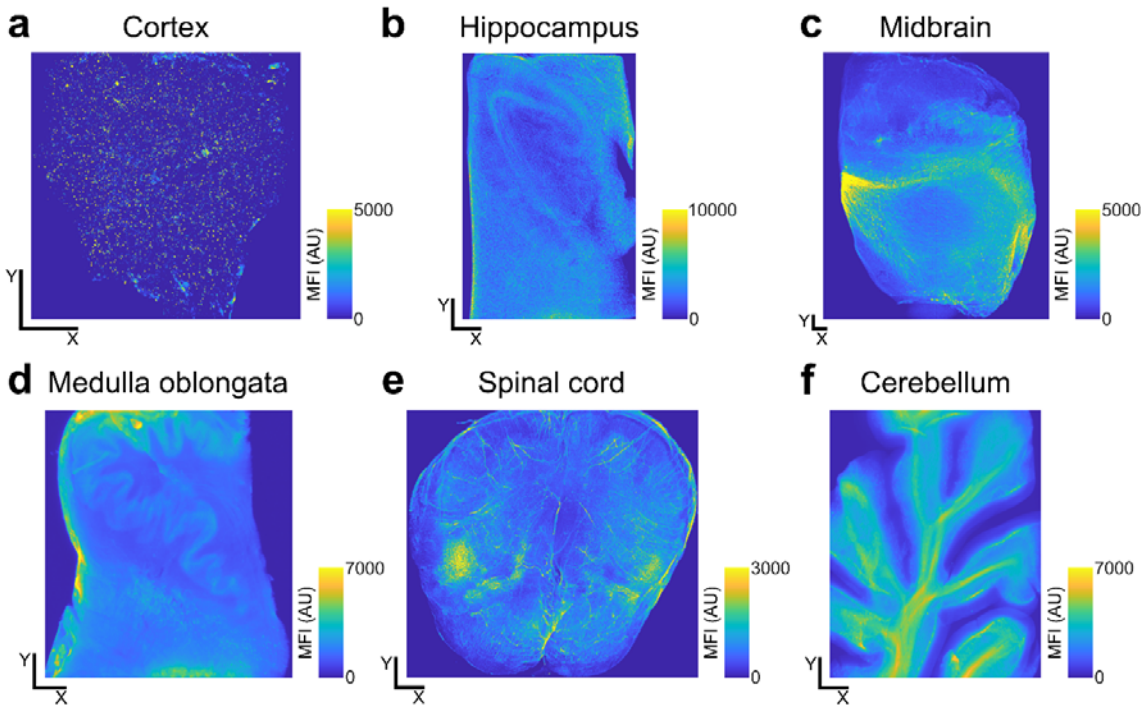


**Extended Data Figure 3. Mean fluorescence intensity projections of different human CNS regions. a-f**, Mean fluorescence intensity (MFI) projections averaged over all planes in z and plotted as heatmaps in xy. Color scales indicate MFI ranges in arbitrary units (AU). Scale bars: 1 mm.

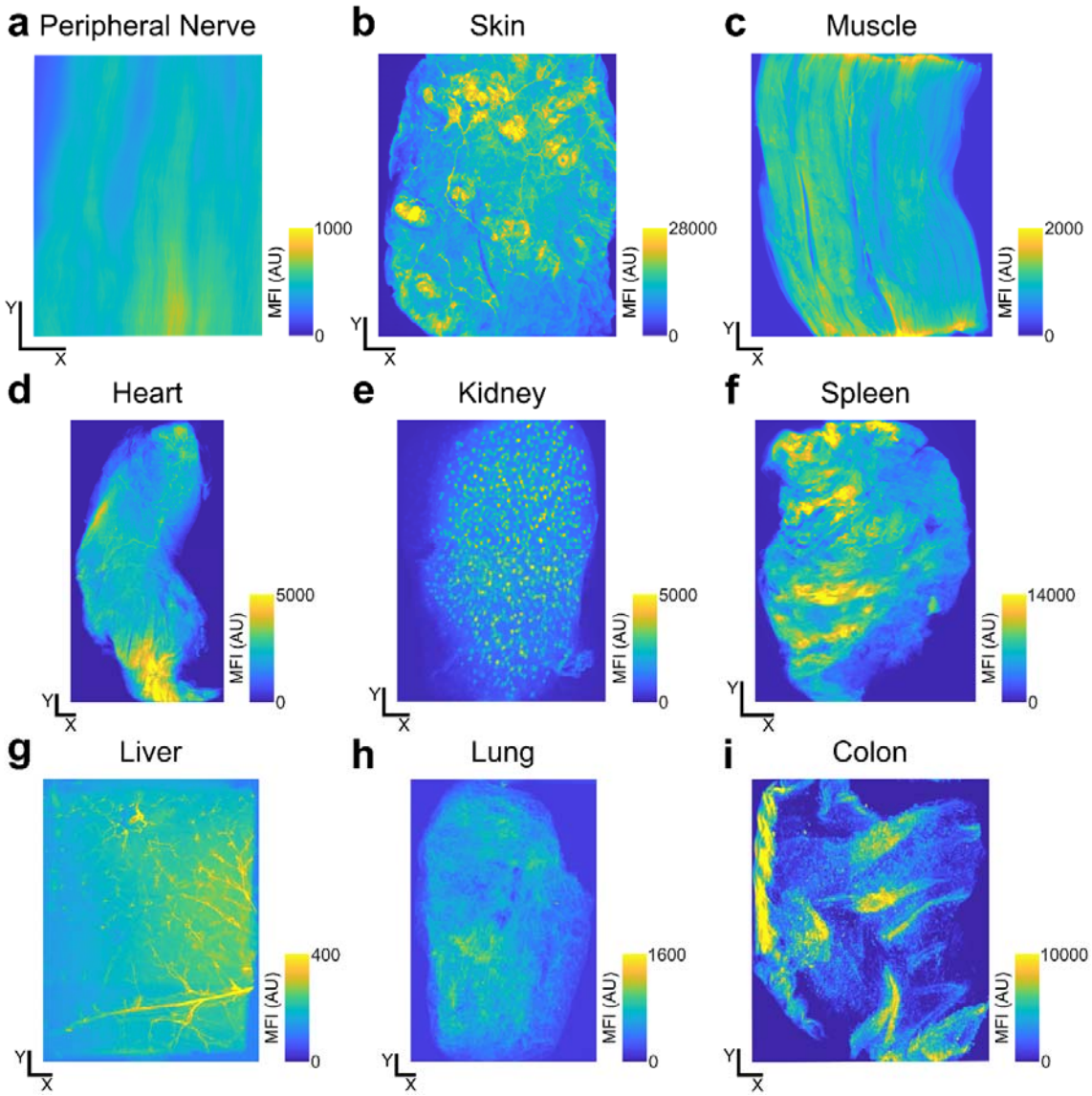


**Extended Data Figure 4. Mean fluorescence intensity projections of different human organs. a-f**, Mean fluorescence intensity (MFI) projections averaged over all planes in z and plotted as heatmaps in xy. Color scales indicate MFI ranges in arbitrary units (AU). Scale bars: 1 mm.

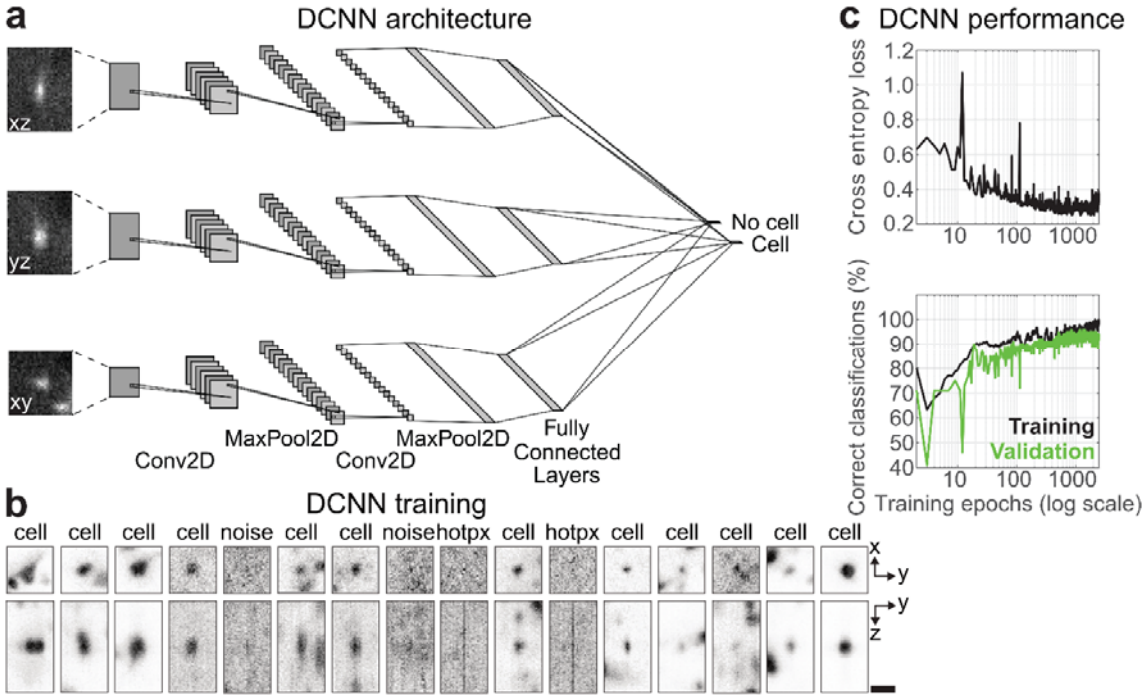


**Extended Data Figure 5. DCNN architecture and performance. a**, DCNN architecture for all three projections xz, yz, and xy. Each network consists of two convolutional (conv) 2D layers with ReLu functions, followed by a 2 x 2 max pooling (pool) 2D layer, two subsequent fully connected layers with ReLu functions, and a final layer with two neurons representing “cell” vs. “non-cell”. The output of the three networks is combined to decide whether a cell candidate is a “cell” or “non-cell”. **b**, DCNN ground truth examples of the training input in different projections to classify “cell” vs. “non-cell” such as noise or hot pixels (hotpx) from the recording camera. For all excerpts, the full side lengths were 46.5 µm x 46.5 µm x 91 µm. Scale bar: 25 µm. **c**, DCNN performance. Top: The cross entropy loss function decays during training and reaches a plateau after 1500 training epochs. Bottom: Percentage of correct classifications increases both for the training set (black) and for the validation set (green), and reaches a plateau of > 90% after 1500 training epochs.

**Extended Data Table 1 | Comparison of human tissue clearing methods**

| | iDISCO (ref.[13]) | DIPCO (ref.[14]) | MASH (ref.[15, 16]) | SHANEL (ref.[17, 18]) | **aDISCO** | OPTI Clear (ref. [19]) | FAST Clear (ref.[20, 21]) | CLARITY (ref.[22, 23]) | SWITCH (ref.[24]) SHIELD (ref.[25]) | HIF (ref.[26]) | ELAST (ref.[27]) | CUBIC (ref.[28]) |
|---|---|---|---|---|---|---|---|---|---|---|---|---|
| FFPE | no | yes | yes | no | **yes** | yes | no | no | no | yes | no | yes |
| Long-term formalin-fixed | no | no | yes | no | **yes** | yes | no | yes | yes | no | yes | no |
| Imaging depth | < 1 mm | 1.6 mm | 3 mm (no Abs) | 1 cm | **6.5 mm** | 546 µm | < 509 µm | 2.6 mm | 100 µm | 900 µm | 5 mm | 2.1 mm (FFPE no Abs), 400 µm (fresh) |
| Ab center homogeneity | yes | yes | NA (no Abs) | no | **yes** | yes | yes | no | yes | yes | no | NA (FFPE no Abs), yes (fresh) |
| Nb. of human organs | 1 | 6 | 2 | 7 | **11** | 1 | 2 | 1 | 1 | 1 | 1 | 2 |
| Nb. of primary antibodies | 2 | 5 | 0 | 10 | **22** | 4 | 3 | 9 | 10 | 3 | 13 | 0 (FFPE), 2 (fresh) |

FFPE: Formalin-fixed paraffin-embedded, Ab: antibody, Nb.: number, NA: not applicable

**Extended Data Table 2 | Characteristics of FCD patients and controls**

| Anonymized patient ID | Age (years) | Gender | Brain localization | Diagnosis | 2D evaluation throughout all layers | Clinical symptoms |
|---|---|---|---|---|---|---|
| 2.2. | 34 | male | right frontal cortex | FCD IIb | no | refractory epilepsy, impulse control disorder, mental retardation |
| 2.3. | 11 | male | right frontal cortex | FCD IIb | no | refractory epilepsy |
| 2.5. | 12 | male | left parietal cortex | FCD IIb (restricted evaluation in 2D) | no | refractory epilepsy |
| 2.6. | 17 | female | right parietal cortex | FCD IIb | yes | refractory epilepsy, attention and lexical/orthographical impairment |
| 2.7. | 48 | male | right parietal cortex | FCD IIb | yes | refractory epilepsy |
| 2.8. | 12 | female | right temporal cortex | FCD IIa | yes | refractory epilepsy |
| 2.10. | 22 | female | right temporal cortex | FCD IIa | no | refractory epilepsy |
| 1.2. | 23 | male | right frontal cortex | control | NA | other (pseudonymized) |
| 1.4. | 11 | male | right frontal cortex | control | NA | other (pseudonymized) |
| 1.5. | 28 | male | right frontal cortex | control | NA | other (pseudonymized) |
| 1.7. | 45 | male | right frontal cortex | control | NA | other (pseudonymized) |
| 1.8. | 33 | female | right frontal cortex | control | NA | other (pseudonymized) |
| 1.9. | 40 | female | right frontal cortex | control | NA | other (pseudonymized) |
| 1.10. | 44 | male | right frontal cortex | control | NA | other (pseudonymized) |

FCD: focal cortical dysplasia, NA: not applicable

**Extended Data Table 3 | Summary of neuronal loss analyses in distinct FCD patients**

| Patient ID | #2 | #3 | #5 | #6 | #7 | #8 | #10 |
|---|---|---|---|---|---|---|---|
| Number of visible lesional foci | 1 | 2 | 11 | 25 | 2 | 5 | 16 |
| Affected volume of brain (%) | 1.25 | 0.41 | 2.65 | 3.67 | 0.06 | 3.98 | 3.32 |
| Affected volume of cortex (%) | 1.46 | 0.46 | 3.05 | 3.77 | 0.08 | 4.43 | 4.02 |
| Affected optical slices (%) | 4.7 | 48.1 | 89.2 | 54.4 | 14.8 | 53.9 | 75.2 |
| Mean affected area fraction per optical slice (%) | 0.73 | 0.27 | 4.00 | 2.47 | 0.05 | 2.73 | 5.02 |
| Cell density (1000 per $mm^3$) | 11.5 | 16.5 | 12.1 | 13.5 | 21.7 | 12.7 | 14.2 |
| Cell density change compared to median density of control (23.7 x 1000 per $mm^3$) | -51.3% | -30.3% | -48.9% | -43.1% | -8.0% | -46.1% | -40.1% |